January 2015

ARABIDOPSIS MYOSIN IS INVOLVED IN THE DISTRIBUTION AND DYNAMIC BEHAVIOR OF THE CELLULOSE SYNTHASE COMPLEX

Chao Cai
Purdue University

Graduate School Form 30
Updated 1/15/2015

PURDUE UNIVERSITY
GRADUATE SCHOOL
Thesis/Dissertation Acceptance

This is to certify that the thesis/dissertation prepared

By Chao Cai

Entitled

Arabidopsis Myosin is Involved in the Distribution and Dynamic Behavior of the Cellulose Synthase Complex

For the degree of Master of Science

Is approved by the final examining committee:

Chris Staiger
Chair

Maureen C. McCann

Dan Szymanski

R. Claudio Aguilar

To the best of my knowledge and as understood by the student in the Thesis/Dissertation Agreement, Publication Delay, and Certification Disclaimer (Graduate School Form 32), this thesis/dissertation adheres to the provisions of Purdue University's "Policy of Integrity in Research" and the use of copyright material.

Approved by Major Professor(s): Chris Staiger

Approved by: Christine Hrycyna 12/4/2015

Head of the Departmental Graduate Program Date

ARABIDOPSIS MYOSIN IS INVOLVED IN THE DISTRIBUTION AND DYNAMIC BEHAVIOR OF THE CELLULOSE SYNTHASE COMPLEX

A Thesis

Submitted to the Faculty

of

Purdue University

by

Chao Cai

In Partial Fulfillment of the

Requirements for the Degree

of

Master of Science

December 2015

Purdue University

West Lafayette, Indiana

To my wife and daughter

ACKNOWLEDGEMENTS

I really appreciate this opportunity to express my gratitude towards people: advisors, lab mates, family and friends who offered help and companionship during my years in graduate school at Purdue.

First, I would really like to thank my research supervisor Dr. Christopher J. Staiger for his massive knowledge in biology, great curiosity in scientific questions, and deep insights in research, which make him a great mentor and role model. I am grateful for his extreme patience in helping me develop the thought process behind hypothesis driven science, guiding me towards proper ways to conduct scientific research, and teaching me to communicate with other scientists efficiently. In addition to Chris, I also want to thank members of my research advisory committee, Drs. Daniel B. Szymanski, R. Claudio Aguilar, and Maureen C. McCann for their time and patience in guiding my scientific thoughts as well as insightful comments and questions during each committee meeting.

Next, I would like to thank Dr. Nicholas C. Carpita and his lab for the help in cell wall component analysis. My knowledge on cell wall biochemistry comes almost entirely from Nick. Thanks to his lab supervisor, Anna Olek, for showing me how to perform the

analysis in cell walls. I am also grateful to Drs. Mike Hahn and Siva Pattathil from CCRC at University of Georgia for their help of carrying out the glycome profiling analysis.

Present and past members of the Staiger Lab have not only provided great support professionally, but were also a group of friends. I am grateful to Jessica Henty-Ridilla, who introduced me to the lab; Jiejie Li, who is a good friend, and has always been cool and thoughtful. Thanks current Staiger Lab members, Hongbing Luo, who always covers my back, and keep my plants alive; Lingyan Cao, who always comes up with great suggestions; Weiwei Zhang, who is really a great collaborator to work with; and Ruthie Arieti, who is also a PULSe student, and is willing to share stories about graduate school with me. Also, I want to thank Ben Staiger, who is not in the lab regularly, but can always offer intelligent insights in mathematics and computer science.

It would be impossible to have accomplished this work without the help from administrative staff members. I would really like to thank Emily Bramson and Karen Sue Malady from the PULSe office for their hard work in smoothing the process of graduate study. Thanks Shelli Taylor for her enthusiasm and help in booking rooms numerous times.

I am also grateful that I always receive great support from family and friends. My parents support every single one of my decisions, only wishing me to be happy. They sacrificed in helping me both financially and emotionally. I really cannot thank my parents more. In addition, I would like to thank my parents-in-law, especially my mother-in-law, who came to the U.S. alone without speaking a single word of English, helping us to get through the hardest time in our lives. Also, I want to thank my dear

friend, Joseph Cox, for introducing me the life in the U.S. and offering companionship, so that I didn't feel quite lonely being so far away from home.

Probably, the best thing that happened to me during these years is marrying a dear friend. Chaonan gave up everything she had back in China, came and joined me here in the U.S., unconditionally supporting my wish to pursue a career in science. She is always optimistic and has faith in me. During these two years we've been in the U.S. together, we really experienced a lot of unforgettable moments, happiness and sorrow, darkest and brightest time in our lives. Words cannot express how much I love my wife.

One of the brightest moments is when time my daughter, Yuxiao, was born. Even though her timing is right at the busiest period of my schedule, I'm still grateful that I have this little angel to cuddle with whenever I came home.

TABLE OF CONTENTS

Page

LIST OF FIGURES

LIST OF ABBREVIATIONS

ADP	Adenosine diphosphate
AP2	Adaptor protein 2 complex
ATP	Adenosine triphosphate
BDM	2,3-butanedione monoxime
BY-2	Bright Yellow 2
CaM	Calmodulin
CESA	Cellulose synthase proteins
CSC	Cellulose synthase complex
CSI1	Cellulose synthase interactive 1
CWM	Cell wall material
DCB	2,6-dichlorobenzonitrile
DMSO	Dimethyl sulfoxide
EM	Electron microscopy
EM-CCD	Electron-multiplying charge-coupled device
fABD	Fimbrin actin-binding domain 2
FLS2	Flagellin-sensitive 2
FP	Fluorescent protein
FRAP	Fluorescence recovery after photobleaching
ISX	Isoxaben
KOR1	KORRIGAN 1
LatB	Latrunculin B
LoG	Laplacian of Gaussian
MASC	Microtubule-associated cellulose synthase compartments
MLC	Myosin light chain
MLCK	Myosin light chain kinase
MyoVin-1	Myosin V inhibitor-1
NEM	N-ethylmaleimide
PBP	Pentabromopseudilin
PEN1	Penetration 1
PM	Plasma membrane
ROI	Region of interest
SDCM	Spinning-disk confocal microscopy

SmaCC	Small CESA compartments
SuS	Sucrose synthase
TFA	Trifluoroacetic acid
TGN/EE	Trans-Golgi network/early endosome
TUB5	β-tubulin 5
VAEM	Variable-angle epifluorescence microscopy
WT	Wild type
xi3KO	*myosin xi-1, xi-2,* and *xi-k* triple knockout mutant
XI-K	Myosin XI-K

ABSTRACT

Cai, Chao. M.S., Purdue University, December 2015. *Arabidopsis* Myosin is Involved in the Distribution and Dynamic Behavior of the Cellulose Synthase Complex . Major Professor: Christopher Staiger.

Plant cells are encased in cell walls which are important for the growth and development of the organism. Primary cell wall consists mainly of polysaccharides with cellulose as the most abundant component. In plant cells, cellulose is synthesized by a plasma membrane (PM) localized protein complex called the cellulose synthase complex (CSC). It was previously reported that disrupting normal actin organization resulted in a reduction of cellulose content in *Arabidopsis* dark-grown seedlings. Furthermore, actin was found to facilitate the delivery of CSC into the PM, and inferred to be involved in endocytosis. As a motor protein that translocates cargo along actin filaments, myosin plays an important role in organelle and vesicle trafficking. However, it is not known whether myosin is involved in regulating cellulose deposition or CSC behavior. Here, we used biochemical analysis to determine the cellulose content in *Arabidopsis* etiolated seedlings, and found a significantly decreased cellulose content in a *myosin xi-1, xi-2,* and *xi-k* triple knockout mutant (*xi3KO*), indicating that myosin is involved in cellulose deposition. To evaluate the molecular mechanism underlying the role of myosin in CSC trafficking, we characterized and employed a new plant myosin inhibitor,

pentabromopseudilin (PBP), which was previously used to inhibit the function of animal and yeast myosins V. With this pharmacological tool, we discovered that treatments with myosin inhibitors reduced the density of CSC at the PM, as well as the rate of delivery of CSC to the PM, which is used to infer that plant myosin is involved in the delivery and internalization of CSC at the PM. Surprisingly, we found that the motility of CSC was significantly inhibited upon treatment with myosin inhibitors, which is different from the results with the actin-polymerization inhibitor Latrunculin B (LatB). Moreover, myosin inhibitor-treated cells showed an altered microtubule orientation, whereas LatB treatment had no effect. These results provide the first evidence that myosin is involved in cellulose deposition and offer insights for the potential mechanism of how myosin regulates CSC behavior.

CHAPTER 1. LITERATURE REVIEW

1.1 Cellulose synthesis and cellulose synthase complex (CSC)

Plants store energy from sunlight through photosynthesis, which provides the expanding population of Earth with energy and nutrition. A large proportion of carbohydrates produced by photosynthesis is used to generate cell wall biomass. The cell wall plays key roles in maintaining many fundamental aspects of plant form and function; for example, it determines the shape of different cell types, holds the cell against turgor pressure, protects plants from pathogenic microbes, and potentially induces defense responses from certain pathogen stimuli (Keegstra, 2010, Somerville, 2006). There are mainly three types of polysaccharides in primary cell walls. Cellulose microfibrils wrap around cells and form the backbone of cell walls. Matrix polysaccharides, including hemicellulose and pectins, bind to and cross-link the parallel cellulose microfibrils, forming a strong network (Scheller & Ulvskov, 2010) and glue neighboring cells together (Harholt et al., 2010).

Cellulose is arguably the most abundant and best-characterized wall component in plant cell walls, as well as the most abundant biopolymer on Earth (Keegstra, 2010). Crystalline cellulose microfibrils consist of a collection of β-1,4-glucan chains that are bundled together by hydrogen bonding (Carpita, 2011, Somerville, 2006). Unlike matrix

polysaccharides, which are synthesized in the Golgi apparatus and delivered into the extracellular space via the secretory pathway, cellulose microfibrils are synthesized from a large transmembrane enzyme complex at the plasma membrane (PM), named the cellulose synthase complex (CSC), and then deposited directly into the extracellular space (Mueller & Brown, 1980, Mueller et al., 1976, McFarlane et al., 2014).

Cellulose synthase can be visualized as symmetrical rosettes of six multiprotein complexes by freeze-fracture, electron microscopy (EM) of PM preparations (Mueller et al., 1976). Each rosette contains a transmembrane domain of about 25~30 nm in diameter, and a much larger catalytic domain of about 50 nm wide (Bowling & Brown Jr, 2008). The CSC rosettes contain cellulose synthase proteins (CESA), demonstrated using immuno-EM by Kimura et al. (1999). CESA was identified originally by homology of a cotton cDNA to bacterial cellulose synthase sequence (Pear et al., 1996), and later on, confirmed by functional analysis of an *Arabidopsis* temperature-sensitive *cesa1* mutant, *rsw1* (Arioli et al., 1998). To form a rosette of 30~36 subunits, at least 3 different types of CESA proteins are required (Taylor et al., 2003). The *Arabidopsis* genome contains 10 CESA genes (Holland et al., 2000, Richmond, 2000). Through the analysis of mutants and antisense constructs, CESA1, CESA3, and CESA6 proteins are found to be necessary for the synthesis of primary cell walls (Fagard et al., 2000, Arioli et al., 1998), with CESA2 and CESA5 displaying partially redundant function to CESA6 (Desprez et al., 2007). On the other hand, CESA4, CESA7, and CESA8 are required for the synthesis of secondary cell walls (Taylor et al., 2003).

1.2 The dynamic behavior of CSC in living cells

In order to study the distribution and dynamic behavior of CSC in living cells, *cesa* mutant plants complemented with functional, fluorescent protein-tagged CESA proteins (FP-CESAs) were generated (Desprez et al., 2007, Paredez et al., 2006, Gutierrez et al., 2009, Watanabe et al., 2015). With FP-CESAs, CSC can be observed at three cellular locations: the Golgi apparatus; small CESA compartments or microtubule-associated cellulose synthase compartments (SmaCC/MASCs); and the PM, which can be distinguished by morphology, localization, and motility patterns (Paredez et al., 2006, Crowell et al., 2009, Gutierrez et al., 2009).

The behavior of CSC at all three locations appears to be dynamic/motile. The motility of CSC-containing Golgi depends upon actin and myosin (Crowell et al., 2009, Gutierrez et al., 2009, Sampathkumar et al., 2013). Disrupting normal actin organization with the actin-polymerization inhibitor latrunculin B (LatB) for 1~4 hours reduces the motility of CSC-containing Golgi apparatus (normally ~0.3 μm/s on average), and also results in Golgi clustering (Gutierrez et al., 2009, Sampathkumar et al., 2013). Small CESA compartments (SmaCCs), also called MASCs, are found to move along microtubules at a rate ~1 μm/min, and their motility is driven primarily by microtubule depolymerization (Crowell et al., 2009, Gutierrez et al., 2009). There is also data suggesting that a subpopulation of subcortical SmaCCs/MASCs move along actin filaments (Sampathkumar et al., 2013) and this will be discussed later. How SmaCCs/MASCs deliver CSC to the PM is currently unknown. While cortical microtubules appear to coincide with the location of CSC insertion, perturbation with oryzalin at moderate

doses does not inhibit the rate of delivery in FRAP experiments (Gutierrez et al., 2009). At the PM, CSCs move along a relatively linear trajectory, co-aligned with cortical microtubules, at a rate ~300 nm/min (Paredez et al., 2006). However, the motility of CSC at the PM, which is originally observed in epidermal cells from 3-d-old etiolated *Arabidopsis* hypocotyls expressing YFP-CESA6, is thought to be powered by the synthesis of cellulose microfibrils (Morgan et al., 2013, Paredez et al., 2006).

Under normal physiological conditions, CSC does not stay at the PM forever. The estimated lifetime of CSC at the PM is ~8 min (Sampathkumar et al., 2013), and then internalized by clathrin-mediated endocytosis (Bashline et al., 2013, Bashline et al., 2015). The internalized CSCs are thought to be substituted by new CSCs that are delivered into the PM (Gutierrez et al., 2009). In coordination with trans-Golgi network/early endosome (TGN/EE), SmaCC/MASCs may serve as a transfer station for the exchange of CSC at the PM (Gutierrez et al., 2009, Crowell et al., 2009, Luo et al., 2015, Sampathkumar et al., 2013). Recent data from Lei et al., 2015 suggest that SmaCCs/MASCs are also involved in the recycling CSC back to the PM. This balance between delivery and internalization of CSC sets up an equilibrium which regulates the density of CSC at the PM (Sampathkumar et al., 2013).

The distribution and dynamic behavior of CSC for cellulose synthesis in the primary and secondary cell walls are different. CSCs were found to be enriched in regions of the plasma membrane associated with bands of cortical microtubules during secondary wall deposition (Watanabe et al., 2015, Wightman & Turner, 2008). Originally, the motility of CSC during secondary cell wall formation was estimated as ten times faster than that in

primary cell wall formation, based on the observation of YFP-CESA7 in root vasculature (Wightman et al., 2009). However, due to the fact that the cells observed for secondary cell wall formation are buried deep inside the tissue, which creates imaging difficulties, the accuracy of the estimation in this study is questionable. Recently, a study of YFP-CESA7 in 3-d-old etiolated hypocotyl epidermal cells that are induced to form ectopic secondary cell walls revealed that the motility of CSC in the PM during secondary cell wall formation is faster than that during primary cell wall formation by up to 1.5 fold (Watanabe et al., 2015). Moreover, the linear density of CSC along individual trajectories at the PM is higher during secondary cell wall formation compared to primary cell wall formation (Watanabe et al., 2015). The faster motility rate, combined with the higher density of CSC at the PM, results in markedly faster cellulose synthesis during secondary cell wall (Watanabe et al., 2015).

1.3 Role of plant cytoskeleton system in regulating CSC behavior

As the key regulator for numerous cellular processes, the plant cytoskeletal system plays important roles in regulating cellulose deposition (McFarlane et al., 2014, Bashline et al., 2014). Cortical microtubules are hypothesized to guide the orientation of cellulose microfibrils (Li et al., 2015, McFarlane et al., 2014, Bashline et al., 2014). Originally, it was found that the orientation of cellulose microfibrils was sensitive to long-term treatment with colchicine, which was later characterized as a microtubule destabilizing drug (Green, 1962). Also, the localization of cortical microtubule appears to be oriented the same as cellulose microfibrils in grazing sections of EM micrographs (Ledbetter &

Porter, 1963). In recent years, visualization of cellulose synthase rosettes (CESA complex) by FP-CESAs shows that the rosettes co-align with, and move along cortical microtubules, even when the dynamic microtubules reoriented (Chan et al., 2010, Paredez et al., 2006). Completely depleting microtubules with 20 μM oryzalin for 7 hours results in a uniformly-dispersed distribution and trajectories of CESA, but no apparent change in CESA motility (Paredez et al., 2006). Thus, microtubules are necessary for orientation of cellulose microfibril deposition but not for cellulose synthesis per se.

The mechanism of the "alignment hypothesis" was partially revealed by the discovery of proteins that interact with both microtubules and CSCs. Cellulose synthase interactive1 (CSI1/POM2) was discovered to directly bind to both CESA subunits and microtubules (Li et al., 2012, Gu et al., 2010, Bringmann et al., 2012). In the *csi1* mutant, CESA trajectories and microtubules are uncoupled, indicating that CSI1 is important for the co-alignment of CSC and microtubules (Bringmann et al., 2012, Mei et al., 2012, Li et al., 2012). Another cellulose synthase interactive protein, CSI3, which is not functionally equivalent to CSI1, also showed a CSC regulatory function in a partial microtubule-dependent manner (Lei et al., 2013).

In addition to microtubules, actin filaments are involved in cellulose deposition (Bashline et al., 2014, McFarlane et al., 2014). During secondary cell wall formation, actin filaments are required for the delivery of CSC to the PM. YFP-CESA7-containing organelles move along actin filaments and pause at delivery sites, and PM-localized CSC bands disappear upon treatment with LatB (Wightman & Turner, 2008). Disrupting actin organization with LatB treatment or an *act2 act7* double mutant causes a significant

reduction in crystalline cellulose content in etiolated seedlings (Sampathkumar et al., 2013). Further, analyses of the distribution and dynamic behavior of CSC in etiolated hypocotyl epidermal cells reveals that actin regulates the dynamic behavior of CSC in Golgi, SmaCC/MASCs, and at the PM. The motility of CSC-containing Golgi was inhibited upon the disruption of actin filaments (Gutierrez et al., 2009, Crowell et al., 2009). In addition to cortical SmaCCs/MASCs that localize 0.3~0.6 μm below the PM focal plane, and move along cortical microtubules, another population of subcortical SmaCCs, which localizes 0.6~1.0 μm below the PM focal plane, has been identified to move along actin filaments (Sampathkumar et al., 2013). Disrupting actin organization causes an increase in the population of microtubule-dependent cortical SmaCCs, as well as abolishes the movement of subcortical SmaCCs (Sampathkumar et al., 2013). Moreover, the delivery (normally at rate ~10 particles/μm^2/h) and internalization (inferred by lifetime) of CSC at the PM are significantly reduced in LatB-treated or *act2 act7* mutant cells, suggesting that actin regulates the delivery and internalization of CSC (Sampathkumar et al., 2013). In these studies, the measurement of CSC density, which is unchanged by disruption of actin, is used to infer the rate of internalization. In addition, the motility rate of CSC at the PM is not altered in actin-disrupted cells, suggesting that the synthesis of cellulose might be independent of actin filaments. Despite the fact that actin filaments are involved in regulating cellulose deposition and CSC behavior, the molecular mechanism of how the actin-dependent delivery and internalization of CSC are driven is currently unknown. As the motor for translocation along actin filaments, myosin is a potential

candidate that could work with actin and provide the driving force for the delivery and internalization of CSC.

1.4 Plant myosin is a potential CSC regulator

Myosin is a huge family of motor proteins that exists ubiquitously in eukaryotic cells (Syamaladevi et al., 2012). One of the first characterized myosins is the conventional myosin II from sarcomeres which slides on actin filaments using the energy of ATP hydrolysis, resulting in muscle contraction (Vale & Milligan, 2000). There are also unconventional myosins in non-muscle cells, most of which function as a molecular motor to transport cargos along actin filaments. There are at least 24 classes of myosin identified among animal, yeast, and plant cells (Foth et al., 2006). Myosin commonly contains two parts: An N-terminal head domain and a C-terminal tail domain (Syamaladevi et al., 2012). The head domain is known as an actin-binding ATPase, which detaches from the actin filament when bound to ATP, and attaches to actin after the ATP is hydrolyzed. The power stroke occurs at the release of P_i from myosin, while it is attached to actin with ADP bound. (Lymn & Taylor, 1971). The tail domain is known as a cargo binding domain, which shows different specificity among different myosins (Li & Nebenführ, 2008). There are two classes of myosin found in higher plants. Class VIII and XI myosins in plants are closely related to class V myosins in animals and yeasts (Hodge et al., 2000, Richards & Cavalier-Smith, 2005). The *Arabidopsis* genome encodes 17 myosin genes with four class VIII *myosins* and thirteen class XI *myosins* (Avisar et al., 2009). Currently, there is no direct evidence supporting that myosin is involved in

cellulose deposition or CESA dynamics, however, some circumstantial evidence may implicate plant myosins in several aspects of CSC behavior. First, several studies demonstrate that myosin activity correlates with the size of plant organs and cells. Studies using *myosin xi* knockout mutants show that the inhibition of growth and size of *Arabidopsis* seedlings directly correlates with the number of myosin genes knocked out (Peremyslov et al., 2010, Ueda et al., 2010). Similarly, organ and cell size are reduced in dark-grown hypocotyls and light-grown roots of a *myosin xi* triple knockout mutant with *myosin xi-1, xi-2,* and *xi-k* (*xi3KO*) knocked out (Cai et al., 2014). Moreover, engineering myosin activity by swapping the head or ATPase domain with faster and slower motors directly correlates with rates of cytoplasmic streaming, plant cell, and organ size; faster myosin results in faster streaming, larger organs and cell size, whereas slower myosin results in slower streaming, smaller organs and cell size (Tominaga et al., 2013).

Second, *Arabidopsis* myosin XI is implicated in callose and lignin-like wall polymer deposition during the response to fungal penetration (Yang et al., 2014). A *myosin xi* quadruple mutant as well as treatment with 2,3-butanedione monoxime (BDM) and N-ethylmaleimide (NEM) (myosin inhibitors) exhibit delayed callose deposition and reduced lignin-like wall polymer deposition in leaf epidermal cells during *Blumeria graminis* infection (Yang et al., 2014). These results are used to infer that plant myosin is involved in cell wall deposition.

Third, actin and myosin are implicated in several examples of exocytosis and endocytosis processes. The motility rate of SCAMP2-labeled secretory vesicles is significantly reduced in *myosin xi* triple knockout mutants, indicating that plant myosin

is involved in the secretory pathway (Peremyslov et al., 2012). Steady-state level secretion of Penetration 1 (PEN1) protein is myosin XI-dependent. The fluorescent intensity of GFP-PEN1 is significantly lower in the *myosin xi* quadruple mutants compared to wild type (WT) (Yang et al., 2014).

Evidence also supports that actin and myosin are involved in endocytosis. The number of FM4-64 stained endosomes is significantly reduced in the *myosin xi* quadruple mutant compared to WT (Yang et al., 2014). Treatment with LatB and BDM inhibit the ligand-induced endocytosis of flagellin receptor, FLS2 (Beck et al., 2012). However, there are contradictory data suggesting that actin filament arrays may also block endocytosis. Disrupting actin organization with LatB treatment actually promoted auxin-induced PIN1 protein internalization (Nagawa et al., 2012). These data suggest multiple mechanisms for the involvement of actin during endocytosis in different biological processes (Li et al., 2014, Baisa et al., 2013).

1.5 The function of plant myosin can be interrogated genetically and pharmacologically

Functions of plant myosin have been tested by numerous groups with genetic approaches by manipulating *myosin* genes. Overexpression of *Arabidopsis* or tobacco myosin XI tail domains in tobacco leaf cells, which causes a dominant-negative effect, inhibits the motility of peroxisomes, Golgi, and mitochondria (Avisar et al., 2008, Sparkes et al., 2008). Similar inhibitory effects on organelle motility were confirmed with *Arabidopsis myosin xi* mutants (Madison et al., 2015, Peremyslov et al., 2010,

Peremyslov et al., 2012, Ueda et al., 2010, Avisar et al., 2008, Ojangu et al., 2012). Moreover, myosin mutant plants are typically stunted and display smaller organs and cell sizes. In addition, the correlation between myosin motility rate and size of plant organ and cell was characterized using genetic approach, as described in the previous section.

Another way to characterize myosin function that has been widely used in plant is pharmacological treatment with myosin inhibitors. Despite the potency of using mutants to study myosin function, there are several problems with the genetic approach to understanding plant myosin function. One issue is that plant genomes contain a large number of myosin genes which are thought to be functionally redundant (Prokhnevsky et al., 2008, Mühlhausen & Kollmar, 2013). Another issue is that plant cells may potentially compensate the function of a mutated gene as a way of dealing with long-term gene loss.

Three drugs, NEM, BDM, and ML-7, are relatively widely used as plant myosin inhibitors. NEM modifies the sulfhydryl group of cysteine residues, and deactivates the motor activity in myosin head domain (Sekine et al., 1962). BDM was originally used as an inhibitor for the ATPase head domain of skeletal myosin II (Herrmann et al., 1992), however, it was subsequently demonstrated to be effective at inhibiting plant myosin XI extracted from *Chara* or lily pollen tube in vitro (Funaki et al., 2004, Tominaga et al., 2000). Although it has been reported that low concentrations of BDM do not inhibit all myosin-dependent cellular processes in plant cells (McCurdy, 1999), it was shown that, at millimolar concentration, BDM can inhibit organelle motility and actin dynamicity

(Nebenführ et al., 1999, Staiger et al., 2009, Cai et al., 2014), which is consistent with the phenotype of *myosin* mutants. ML-7 is an inhibitor of myosin light chain kinase from smooth muscle (Saitoh et al., 1987). The assumed mechanism of ML-7 in plant cells is that it can inhibit the putative plant myosin light chain phosphorylation, which reduces the activity of myosin (Molchan et al., 2002). Despite the fact that there is limited information on the effectiveness and specificity of these drugs on plant myosin, most recent studies confirm their pharmacological results with two to three drugs treatment, or by combining with genetic studies. Despite potential problems, there are benefits of pharmacological studies. Inhibitor treatment offers acute poisoning of the motor, which allows us to study the motor activity in a short-term and dose-dependent manner

Recently, new inhibitors of animal myosin V have been discovered, which could be potential candidates as plant myosin inhibitors. Pentabromopseudilin (PBP) reduces the rate constants for ATP binding, ATP hydrolysis and ADP dissociation from the myosin ATPase domain, as well as inhibits myosin V-dependent processes in budding yeast (Fedorov et al., 2009, Preller et al., 2011). Myosin V inhibitor-1 (MyoVin-1) can specifically inhibit ADP release from the actomyosin complex in an uncompetitive mechanism, thus slowing the actin-activated myosin V ATPase (Islam et al., 2010). Given that plant myosin proteins are close relatives of myosin V in animals and yeast (Richards & Cavalier-Smith, 2005, Mühlhausen & Kollmar, 2013), these drugs could be promising supplements for BDM in plant myosin studies.

To gain a better understanding of how myosin might regulate cellulose deposition and cell wall assembly, we hypothesize that plant myosin is involved in regulating the

distribution and dynamic behavior of CSC. To test this hypothesis, we used myosin inhibitors, combined with spinning-disk confocal imaging of living plant epidermal cells expressing YFP-CESA6 (in *prc1-1* mutant background). Quantitative analysis of CESA density at the PM, delivery rates, and velocity of movement during celluloses synthesis, revealed that plant myosin facilitates the delivery and internalization of CSC at the PM, as well as the rate of CSC motility.

CHAPTER 2. METHODS AND MATERIALS

2.1 Plant materials and growth conditions

The *Arabidopsis* mutant with *myosin xi-1, xi-2,* and *xi-k* knocked out (*xi3KO*) and the *xi3KO* mutant expressing vYFP-fABD2 were characterized previously (Peremyslov et al., 2010). For Golgi and actin analysis, YFP-tagged Mannosidase I (YFP-ManI) and GFP-tagged second actin-binding domain from *Arabidopsis* Fimbrin 1 (GFP-fABD2) seeds were from Staiger lab stocks (Sheahan et al., 2004, Nebenführ et al., 1999). For CSC imaging, the *prc1-1* homozygous mutant expressing YFP-cellulose synthase 6 (YFP-CESA6) seeds were propagated from a previously characterized stock (Paredez et al., 2006, Li et al., 2012, Bashline et al., 2013), kindly provided by Ying Gu (Pennsylvaina State University). Seeds were surface sterilized and stratified at 4°C for 3 days on half-strength Murashige and Skoog (MS) medium supplemented with 1% sucrose and 1% agar. After 4 h of exposure to light, plates were wrapped in three layers of aluminum foil and placed in continuous darkness. Three- to five-d-old seedlings used for cell wall determination and CSC imaging were grown vertically, and seedlings used for Golgi motility and actin analysis were grown horizontally at 21°C.

2.2 Drug treatment

Latrunculin B (LatB), butanedione monoxime (BDM), isoxaben (ISX), and 2,6-dichlorobenzonitrile (DCB) were purchased from Sigma-Aldrich. Pentabromopseudilin (PBP) was purchased from Adipogen Corporation. MyoVin-1 was purchased from EMD Millipore.

For cellulose content and monosaccharide composition analysis, wild-type seedlings were grown on ½ MS plates containing 100 nM LatB. For Golgi motility assay as well as actin architecture and dynamics analyses, hypocotyls were pretreated for 15 min with mock (0.2% DMSO), 30 mM BDM, 10 μM PBP (from 2.5 mM stock solution in DMSO), or 20 μM MyoVin-1 (from 5 mM stock solution in DMSO), and then mounted in corresponding solutions for imaging. For CSC density, CSC motility, and microtubule orientation analysis, hypocotyls were pretreated for 15 min with mock (0.2% DMSO), 10 μM LatB (from 5 mM stock solution in DMSO), 30 mM BDM, 10 μM PBP, 100 nM ISX (from 100 mM stock solution in DMSO), or 5 μM DCB (from 5 mM stock solution in DMSO), and mounted in corresponding solutions for imaging. For CSC delivery analysis, hypocotyls were mounted in mock (0.2% DMSO), 10 μM LatB, 30 mM BDM, 10 μM PBP, 100 μM PBP (from 25 mM stock solution in DMSO), 100 nM ISX, or 5 μM DCB, and imaged immediately.

2.3 Cell wall determination

Five-d-old hypocotyls were lyophilized and then ground in SDS buffer (1% SDS, 50 mM Tris-HCl, pH 7.2). The homogenate was washed sequentially with SDS buffer and 50%

ethanol at 60°C, and then with distilled water at ambient temperature. The sample was pelleted at 4,500 rpm, and considered as cell wall material (CWM).

The amount of cellulose in CWM from etiolated *Arabidopsis* hypocotyls was determined by a method modified from Updegraff, 1969. CWM was resuspended with 0.9 mL distilled water, and 0.1 mL sample was taken for total sugar analysis. The rest of the sample was transferred into glass conical vials. For total cellulose determination, the non-cellulosic portion of CWM was hydrolyzed with 2 M TFA (containing 500 µM myo-inositol as internal standard for monosaccharide analysis) at 120°C for 90 min. For crystalline cellulose determination, the non-cellulosic portion of CWM was hydrolyzed with acetic nitric reagent (acetic acid : nitric acid : water = 8:1:2) at 100°C for 60 min. The residue from hydrolysis was then washed with distilled water and aliquoted into three technical repeats. The amount of sugar in samples was measured using phenol sulfuric colorimetric assay (Dubois et al., 1956). In a test tube, 200 µL test sample and 200 µL 5% (v/v) phenol were mixed together, then 2 mL concentrated sulfuric acid was introduced to develop color. After overnight incubation, $O.D._{500}$ was read, and then converted to weight by comparing to a standard curve generated from a known amount of cellulose (Dubois et al., 1956).

To analyze the monosaccharide composition in CWM, the supernatant from TFA hydrolyzed samples was transferred into a small flat-bottom screw-cap tube, and mixed 1:1 with tert-butanol, then dried under nitrogen gas overnight. After the sample was completely dried, 0.5 mL freshly-made 20 mg/mL $NaBH_4$ in DMSO and 0.1 mL 1 M $NH_3{\cdot}H_2O$ was added, and incubated in a water bath at 40~45 °C for 90 min. The

reduction reaction was stopped by neutralizing with 100 µL glacial acetic acid, followed by 100 µL 1-methylimidazole. To generate alditol acetates, 750 µL anhydrous acetic anhydride was added into the sample, mixed thoroughly and incubated at 40~45 °C for 30 min. The reaction was stopped by adding 1.5 mL distilled water. The alditol acetate was extracted with dichloromethane, and washed multiple times with distilled water before evaporated dichloromethane at 40~45 °C. The samples were then re-dissolved in 500 µL dichloromethane, and then run through gas chromatography–mass spectrometry. The amount of each monosaccharide was calculated based on the proportional area under the corresponding peak comparing to the internal control (myo-inositol)(Carpita & Shea, 1989).

2.4 Live-cell imaging

For imaging Golgi and actin filaments in 5-d-old etiolated hypocotyl epidermal cells, variable-angle epifluorescence microscopy (VAEM) was performed using a TIRF illuminator on an IX-71 microscope (Olympus), equipped with a 60×1.45–numerical aperture PlanApo TIRF objective (Olympus). Both YFP-ManI and GFP-fABD2 were excited with a 488-nm laser line from a solid-state 50 mW laser (Intelligent Imaging Innovations), and emitted through a 525/30-nm filter, and captured with an EM-CCD camera (ORCA-EM C9100-12; Hamamatsu Photonics). Time-lapse series for Golgi motility were taken at 500-ms intervals for 121 frames, and for actin dynamics were taken at 1-s interval for 100 frames. The VAEM platform was operated with Slidebook software (version 6.0; Intelligent Imaging Innovations). For CSC density, motility, and microtubule imaging,

spinning-disk confocal microscopy (SDCM) was performed using a Yokogawa scanner unit CSU-X1-A1 on an Olympus IX-83 microscope, equipped with a 100×1.4–numerical aperture UPlanSApo oil objective (Olympus). YFP-CESA6 and YFP-TUB5 were excited with a 514-nm laser, and emitted through a 542/27-nm filter, and captured with an Andor iXon Ultra 897BV EMCCD camera (Andor Technology). For CSC density and motility imaging, time-lapse images were collected at the plasma membrane with a 5-s interval for 5 or 61 frames, respectively. For microtubule analyses, images from a single focal plane were collected. The SDCM platform was operated with MetaMorph software (version 7.8.8.0; Molecular Devices)

For fluorescence recovery after photobleaching (FRAP) experiments, images were collected with a Zeiss Observer Z.1 microscope, equipped with a Yokogawa CSU-X1 and a 100×1.46–numerical aperture PlanApo objective (Zeiss). YFP-CESA6 was excited with a 515-nm laser line, and emitted through a 525/50 filter. Photobleaching was performed with a Vector scanner (Intelligent Imaging Innovations) with a 515-nm laser line at 100% power and 3 ms/scan. Time-lapse images were collected at the plasma membrane with a 5-s interval for 150 frames, with photobleaching in a region of interest (ROI) of 16 µm (100 pixels) in diameter after the 6^{th} frame, and recovery monitored for a total of 12.5 min. The FRAP platform was operated with Slidebook software (version 6.0; Intelligent Imaging Innovations).

2.5 Image processing and quantitative analysis

Image processing and analysis were generally performed with ImageJ (version 1.5b), and will be mentioned specifically otherwise.

For Golgi motility analysis, time-lapse series were converted to 8-bit, and run through "TrackMate" plugin with Laplacian of Gaussian (LoG) algorithm as particle detection filter. Trajectories detected by TrackMate were selected for analysis only if more than 5 spots were on the trajectory and the mean trajectory quality was greater than 20. The parameter "Mean Speed" was then pooled, and plotted as the average Golgi motility rate.

The analyses of actin architecture and dynamics followed the description in Cai et al., 2014. For actin architecture analysis (filament abundance and extent of bundling), micrographs were cropped and converted to 8-bit. A custom macro written by Benjamin Staiger (Purdue University), combining the "skewness" and "density" algorithm originally from Higaki et al., 2010, was applied for image analysis. Overall actin dynamicity analyses were performed in MATLAB (version 7.14.0, MathWorks) using the method described in Vidali et al., 2010. Pair-wise Pearson correlation coefficient was calculated for all the possible time intervals sequentially. For the analysis of filament shape change, single actin filaments were hand tracked from time-lapse series generated for overall actin dynamicity analysis. Convolutedness and the rate of change of convolutedness were measured for actin filament shape change. Convolutedness is defined as the ratio of filament length divided by the Euclidean distance. The rate of

change of convolutedness is the average difference in convolutedness between consecutive frames divided by the time interval between frames.

For the analysis of CSC distribution and dynamic behavior, background was subtracted using “Subtract Background” in ImageJ with rolling ball radius set at 30 pixels. Images were then cropped and converted to 8-bit for further analysis. For CSC density measurements, time projections were generated from five successive frames at 5-s intervals with “average intensity” algorithm in order to maximize the visualization of CSC at plasma membrane. The number of CSC was then counted with the LoG detector in TrackMate using the time projections. CSC density was calculated as the number of particles detected divided by the area of ROI.

For CSC delivery analysis, an ROI was selected at the center of bleached area with a diameter of 12.8 μm (smaller than bleached area) to exclude the lateral movement of CSC into the bleached region (Sampathkumar et al., 2013). The density of CSC in the ROI was measured as described above. The CSC delivery rate was calculated as the slope of linear regression line from the first three minutes after photobleaching. CSC lifetime was calculated as density (from CSC density analysis) divided by delivery rate (Sampathkumar et al., 2013). For CSC motility rate measurements, kymographs were generated by following a trajectory of CSC particles in the time-lapse series. CSC motility rate was calculated as the reciprocal of the slope of individual CSC particles in kymographs (Paredez et al., 2006).

The orientation of microtubules was analyzed based on the methods described in Ueda et al., 2010 and Cai et al., 2014. Images were rotated with longitudinal cell axis parallel

to the horizontal axis of the image, and then skeletonized through a bandpass filter. Average angle of microtubules with respect to the longitudinal cell axis and the parallelness of microtubules with respect to each other were measured with a custom written macro by Benjamin Staiger, which coordinates procedures within the kbi plugin (http://hasezawa.ib.k.u-tokyo.ac.jp/zp/Kbi/ImageJKbiPlugins).

2.6 Statistical analysis

Statistical analyses were performed using Excel (version 14.0.6112.500, Microsoft), MATLAB (version 7.14.0, MathWorks), or R (version 3.2.2).

CHAPTER 3. RESULTS

3.1 Cellulose content is reduced in the *myosin xi3KO* mutant

Recently, it was reported that *Arabidopsis* myosin is involved in regulating cell size, exocytosis, and cell wall deposition (Cai et al., 2014, Peremyslov et al., 2010, Tominaga et al., 2013, Yang et al., 2014). To test whether plant myosin regulates cellulose deposition, we measured cellulose content in a previously characterized mutant with *myosin xi-1*, *myosin xi-2*, and *myosin xi-k* knocked out (*xi3KO*) (Peremyslov et al., 2010). To determine the cellulose content, we prepared an alcohol-insoluble cell wall fraction and hydrolyzed non-cellulosic cell wall components with trifluoroacetic acid (TFA) (Gibeaut & Carpita, 1991) or acetic nitric (AN) reagent (Updegraff, 1969). The amount of cellulose in the residual fraction was measured with the phenol sulfuric colorimetric assay (Dubois et al., 1956). With TFA hydrolysis, both amorphous and crystalline cellulose would be left in the residue, however, AN reagent can also hydrolyze amorphous cellulose, leaving mainly the crystalline fraction (Updegraff, 1969). The *xi3KO* mutant had a significantly reduced cellulose content compared to the wild type (WT) control (Figure 3.1, A to D). Similarly, wild-type seedlings grown on medium containing the actin-polymerization inhibitor latrunculin B (LatB) showed a decrease in cellulose content (Figure 3.1, A to D), which is consistent with a previous study

(Sampathkumar et al., 2013). This result demonstrates that plant myosin is involved in cellulose deposition.

In addition to cellulose content, we also analyzed cell wall monosaccharide composition to test whether non-cellulosic cell wall components were altered in the *xi3KO* mutant. The amount of monosaccharides was measured with gas chromatography-mass spectrometry from alditol acetates generated from the TFA-soluble cell wall fraction (Gibeaut & Carpita, 1991). There were no significant differences in amounts of individual monosaccharides with LatB treatment or in the xi3KO mutant (Figure 3.1E).

3.2 Validation of PBP as a myosin inhibitor in plant cells

Butanedione monoxime (BDM) is the most commonly used myosin inhibitor in plants, but its mode of action has been questioned (McCurdy, 1999). Pentabromopseudilin (PBP) and MyoVin-1 are potent inhibitors of myosin V in animal cells (Fedorov et al., 2009, Islam et al., 2010). Moreover, PBP inhibits the myosin-dependent polarized distribution of mitochondria in budding yeast, indicating a cross-kingdom effectiveness (Fedorov et al., 2009). Considering that both plant class VIII and XI myosins are closely related to class V myosins (Hodge et al., 2000, Mühlhausen & Kollmar, 2013), PBP and MyoVin-1 may be potential candidates as plant myosin inhibitors. To test this, we measured Golgi motility, which has been characterized primarily as a myosin XI-dependent cellular process (Peremyslov et al., 2008, Peremyslov et al., 2010, Prokhnevsky et al., 2008). To measure Golgi motility, time-lapse series were collected from 5-d-old etiolated hypocotyls expressing YFP-Mannosidase I (YFP-ManI) with variable-angle

epifluorescence microscopy (VAEM). Hypocotyls were treated for 15 min with mock, 30 mM BDM, 10 µM PBP, or 20 µM MyoVin-1 prior to imaging. Two types of Golgi movement in epidermal cells have been described, with fast directional movement supported by actin bundles and regional wiggling presumably trapped by actin meshwork (Akkerman et al., 2011). Representative time projections which display the trajectories of Golgi motility showed a directional fast Golgi movement upon mock and MyoVin-1 treatment (Figure 3.2, A and B), however, in BDM and PBP treated cells, the majority of Golgi wiggled in a confined area (Figure 3.2, A and B). Quantitative analysis of Golgi motility showed a significant reduction in rates upon BDM and PBP treatment compared to mock treatment, but no significant difference was detected following MyoVin-1 treatment (Figure 3.2C). This result indicates that PBP can effectively reduce Golgi motility, and validates its use as a myosin inhibitor in plants.

We also examined actin organization and dynamic behavior, which were found to be myosin dependent previously (Cai et al., 2014, Park & Nebenführ, 2013). It has been shown that the overall actin dynamicity in *Arabidopsis* hypocotyl epidermal cells was reduced in the *xi3KO* mutant, and that myosin generates forces for the buckling and straightening of actin filaments (Cai et al., 2014). Representative images of epidermal cells from hypocotyls expressing the actin reporter GFP-fABD2 (Sheahan et al., 2004) showed that the cortical actin array was more dense in BDM-treated cells compared to mock treatment, but there were no obvious changes in PBP- or MyoVin-1-treated cells (Figure 3.3A). Quantitative analyses were performed to analyze the architecture of cortical actin arrays. Skewness and density were measured to evaluate the extent of

bundling and the percentage of occupancy of actin filaments in epidermal cells respectively (Higaki et al., 2010, Henty et al., 2011). Cells treated with BDM had a significantly increased percentage of occupancy and slightly reduced bundling of actin arrays compared to mock treatment; however, no significant differences were detected following PBP or MyoVin-1 treatment (Figure 3.3, B and C).

In addition to myosin inhibitors, we also validated the effectiveness of LatB treatment in disrupting cortical actin arrays. Cells treated with 100 nM or 10 µM LatB for 15 min showed fragmented actin filament arrays, as well as decreased filament abundance (Figure 3.4A). Quantitative analysis of actin architecture revealed that the percentage of occupancy was reduced in a LatB-dependent manner (Figure 3.4B). Extent of bundling was increased after the treatment with 10 µM LatB (Figure 3.4C). These results suggested that short-term LatB treatment can disrupt, but not abolish, cortical actin filament arrays.

To analyze whether actin dynamics were altered by treatment with potential myosin inhibitors, time-lapse series were collected. We first quantified overall actin dynamicity by calculating the correlation coefficient of pixel intensity for all pairwise temporal intervals (Vidali et al., 2010). The correlation coefficient curves for BDM and PBP treatment decayed significantly slower compared to mock and MyoVin-1 treatment (Figure 3.3D), indicating a decreased overall actin dynamicity in the presence of myosin inhibitors. Convolutedness and the rate of change of convolutedness were measured to test whether myosin-dependent actin buckling and straightening are altered by the treatment with potential myosin inhibitors (Cai et al., 2014). The convolutedness of

single actin filaments showed no difference after BDM, PBP, or MyoVin-1 treatment compared to mock (Figure 3.3E). However, BDM and PBP treatment caused a significant reduction in the rate of change of convolutedness (Figure 3.3F), indicating that filament buckling and straightening was reduced following the treatment with PBP and confirms previous results with BDM (Cai et al., 2014). These results showed that PBP can inhibit multiple myosin-dependent processes, and thus could be a potential candidate as a myosin inhibitor in plants. MyoVin-1, on the other hand, seems not to affect myosin-dependent processes in plant cells; we therefore forego further use in this study.

3.3 Apparent CSC density at the plasma membrane is reduced after myosin inhibitor treatment

One possible explanation for the reduction of cellulose content in the *xi3KO* mutant is that the amount of CSCs at the plasma membrane (PM), available for cellulose synthesis, is decreased in the absence of myosin activity. We analyzed the distribution and dynamic behavior of CSC using *Arabidopsis* plants expressing functional YFP-CESA6 that complemented a *prc1-1* mutant (Paredez et al., 2006). To test whether myosin activity is involved in regulating CSC density at the PM, we examined the distribution of PM-localized CSC in response to myosin inhibitor treatment using time-lapse spinning-disk confocal microscopy (SDCM). Time projections were generated to enhance the detection of CSC, based on the slow motility of CSC at the PM (Paredez et al., 2006). Representative time projections showed a reduced amount of CSCs upon BDM and PBP treatment (Figure 3.5, A and B). Quantitative analysis of the number of CSCs showed

that, in mock-treated epidermal cells, CSCs density was 1.32 ± 0.03 particles/μm^2 (Figure 3.5C), which is consistent with a value of 1.34 ± 0.08 particles/μm^2 observed by Sampathkumar et al., 2013. A significant reduction of CSC density upon treatment with BDM and PBP compared to mock treatment was observed (Figure 3.5C). In contrast, treatment with the actin-polymerization inhibitor LatB as well as the cellulose synthase inhibitor 2,6-dichlorobenzonitrile (DCB), had no significant effect on CSC density, whereas another cellulose synthesis inhibitor isoxaben (ISX) showed a decrease in CSC density compared to mock treatment (Figure 3.5, A-C). The results with LatB and ISX are consistent with previous studies (Sampathkumar et al., 2013, DeBolt et al., 2007, Gutierrez et al., 2009). Our new data suggest that myosin is involved in regulating the abundance of CSC at the PM.

3.4 Rate of delivery and apparent lifetime of CSC at the PM are affected by myosin inhibitors

The density of CSC at the PM is regulated by the dynamic balance of delivery and internalization (Bashline et al., 2013, Bashline et al., 2015). It was reported that disrupting actin organization genetically and pharmacologically could hinder both the delivery and uptake of CSC at PM (Sampathkumar et al., 2013). As a motor protein that translocates organelles and vesicles along actin filaments, myosin could possibly be involved in exocytosis, endocytosis, or both. Thus, we hypothesized that the reduction of CSC density at the PM upon myosin inhibitor treatment is due to the disruption of the balance between delivery and internalization of CSC. Fluorescence recovery after

photobleaching (FRAP) experiments have been applied in several studies to analyze the rate of delivery of CSC to the PM (Sampathkumar et al., 2013, Bashline et al., 2013, Gutierrez et al., 2009). To avoid error that may be introduced through lateral movement of CSCs, we analyzed a region of interest (ROI) that is smaller than the bleached area (Figure 3.6A) (Sampathkumar et al., 2013). By counting the number of CSC particles in ROIs after photobleaching, we observed that the recovery of CSCs in the bleached area was slower upon LatB, BDM, and PBP treatment compared to mock treatment (Figure 3.6B). Indeed, a higher concentration of PBP (100 μM) showed even greater inhibition of recovery than did 10 μM PBP (Figure 3.6B). The delivery rate of CSC to the PM was calculated as the slope of linear regression during the initial 3 min of recovery (Sampathkumar et al., 2013). In mock-treated epidermal cells, CSCs were delivered at a rate of 0.22 ± 0.02 particles/μm^2/min (Figure 3.6C), which is consistent with a value of 0.19 ± 0.02 particles/μm^2/min observed by Sampathkumar et al., 2013. Epidermal cells treated with LatB, BDM, and PBP had significantly decreased delivery rates compared to mock treatment (Figure 3.6C). In addition, PBP showed inhibition of CSC delivery in a dose-dependent manner (Figure 3.6C). Despite the fact that there is no direct measurement for the internalization rate of CSC, calculated lifetime using density divided by delivery rate has been adapted to estimate the endocytosis of CSC (Sampathkumar et al., 2013). The calculated lifetime was significantly extended upon the treatment with LatB, BDM, and PBP compared to mock treatment (Figure 3.6D). However, LatB was more potent than both myosin inhibitors, which had CSC lifetimes only slightly greater than mock treatment. As controls, CSC inhibitors, ISX and DCB,

showed a significant decrease in CSC delivery rate and a marked increase in lifetime. These results indicate that plant myosin is involved in regulating both the delivery and internalization of CSC at the PM.

3.5 Motility rate of CSC at the PM is reduced by myosin inhibitors

In addition to the amount of CSC at the PM, the rate of cellulose synthesis can also affect cellulose content. Given that the synthesis of cellulose microfibrils is thought to be the driving force for motility of CSCs at the PM (Morgan et al., 2013, Paredez et al., 2006), we analyzed the rate of motility of CSCs as an indirect measurement to test whether the CESA activity was altered. To test whether myosin could regulate CSC motility, time-lapse series were obtained with SDCM, and time projections were generated to visualize the trajectories of CSC motility (Figure 3.7A). Representative time projections and kymographs showed that CSCs traveled bidirectionally on linear trajectories in mock- and LatB-treated cells. However, the trajectories in BDM- and PBP-treated cells are not quite visible, suggesting that the motility was lowered (Figure 3.7, A and B). Quantitative analysis of CSC motility using kymographs (Paredez et al., 2006) revealed that BDM and PBP treatments had significantly reduced CSC motility rates compared to mock and LatB treatments (Figure 3.7, B and C). ISX and DCB treatments also inhibited CSC motility significantly, as reported in a previous study (DeBolt et al., 2007). These results indicate that myosin influences CESA activity.

3.6 Microtubule orientation is altered upon treatment of myosin inhibitors

One of the factors that coordinates the motility of CSC at the PM is the cortical microtubule array. Microtubules guide the trajectories of CSC motility (Paredez et al., 2006, Chan et al., 2010). There is genetic and pharmacological evidence suggesting that CESA activity can influence microtubule orientation and stability (Persson et al., 2007). Thus, we hypothesized that altering CSC distribution and dynamic behavior with myosin inhibitors can alter microtubule orientation. To test this hypothesis, we examined microtubule organization in epidermal cells from 3-d-old etiolated hypocotyls expressing yellow fluorescent protein tagged β-tubulin 5 (YFP-TUB5) (Shaw et al., 2003, Staiger et al., 2009). Representative images showed that microtubules were mainly oriented transverse to the longitudinal axis of the cell in both mock- and LatB-treated cells (Figure 3.8A). However, treatment with myosin inhibitors resulted in microtubule orientations that were oblique (PBP) or even parallel (BDM) to the longitudinal cell axis (Figure 3.8A). Quantitative analyses of the average angle of microtubules against the longitudinal axis of cells (Cai et al., 2014, Ueda et al., 2010) showed that BDM and PBP treatment had a significantly decreased angle compared to mock and LatB treatment, confirming that microtubule orientation changed more longitudinally upon treatment with myosin inhibitors (Figure 3.8B). Parallelness of microtubules with respect to each other was also measured (Cai et al., 2014, Ueda et al., 2010). PBP treatment showed a significantly decreased parallelness compared to mock treatment, indicating a less ordered microtubule array after PBP treatment (Figure 3.8C). However, BDM showed an increase

in parallelness compared to mock treatment (Figure 3.8C). These results demonstrate for the first time that myosin can influence microtubule organization.

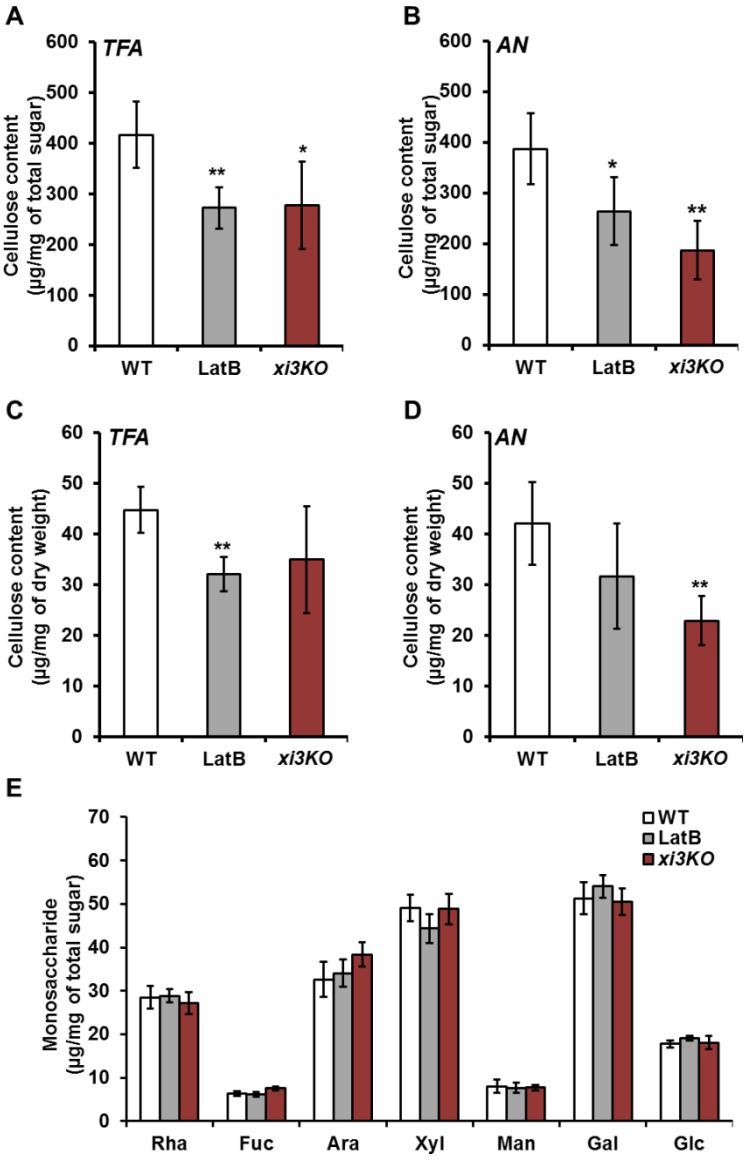

Figure 3.1. Cellulose content is reduced in the *myosin xi3KO* mutant.

Figure 3.1. Cellulose content is reduced in the *myosin xi3KO* mutant.
Ethanol-insoluble cell wall material (CWM) was prepared from 5-d-old etiolated hypocotyls of wild-type Col-0 (WT), the *myosin xi3KO* mutant, and WT growing on plates containing 100 nM latrunculin B (LatB). (A to D) Cellulose content was measured. The non-cellulosic component of CWM was hydrolyzed with 2 M trifluoroacetic acid (TFA; A and C) or acetic nitric reagent (AN; B and D). The amount of cellulose and total sugar were then determined by a phenol sulfuric colorimetric assay and converted to weight amounts for determination. Cellulose content was plotted as the ratio of total sugar (A and B) or dry weight (C and D). The cellulose content was significantly reduced in LatB-treated and *xi3KO* mutant hypocotyls compared to WT. Values given are means ± SD (n = 4 biological repeats; Student's t test, *P <0.05, **P < 0.01). (E) Monosaccharide composition was analyzed by gas chromatography-mass spectrometry (GC-MS) with alditol acetates generated from the TFA-soluble fraction of CWM. There were no significant differences in amounts of individual monosaccharides. Values given are means ± SD (n = 4; Student's t test, P > 0.05).

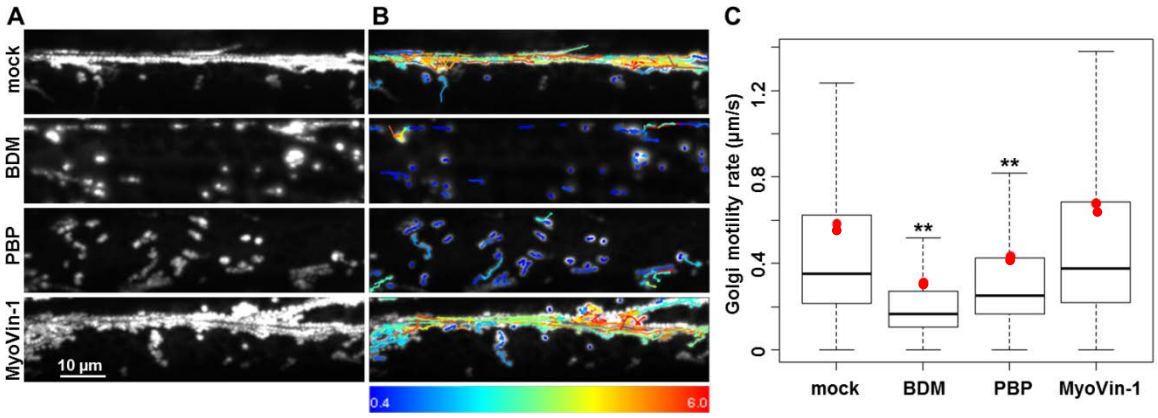

Figure 3.2. Myosin inhibitor treatments reduce Golgi motility in hypocotyl epidermal cells.

(A) Representative time projections show the trajectories of Golgi motility from 5-d-old etiolated hypocotyls expressing YFP-Mannosidase I (YFP-ManI). Hypocotyls were treated for 15 min with mock (0.2% DMSO), 30 mM 2,3-butanedione monoxime (BDM), 10 µM pentabromopseudilin (PBP), or 20 µM MyoVin-1 prior to imaging. Variable-angle fluorescent microscopy (VAEM) time-lapse series were collected from epidermal cells in the basal region of the hypocotyl at 0.5-s intervals for 121 frames. Time projections were generated with maximum intensity of all 121 images. Bar = 10 µm. (B) Trajectories of Golgi motility detected with ImageJ plugin "TrackMate" in (A). Heat map of trajectories indicates the maximum speed from 0.4 to 6 µm/s. (C) Box-whisker plots show Golgi motility in inhibitor-treated epidermal cells. The body of the box consists of median, the first and third quartiles. Whiskers represent 1.5 times of inter-quartile range (IQR) above or below the first and third quartiles, respectively. Outliers are not shown in the plot. Red solid circles show the average Golgi motility rates. The rate of Golgi motility was significantly decreased after BDM and PBP treatments, whereas MyoVin-1 had little or no effect. Values given are means ± SE (n > 5000 trajectories from 20 hypocotyls per treatment; Student's t test, **P < 0.01).

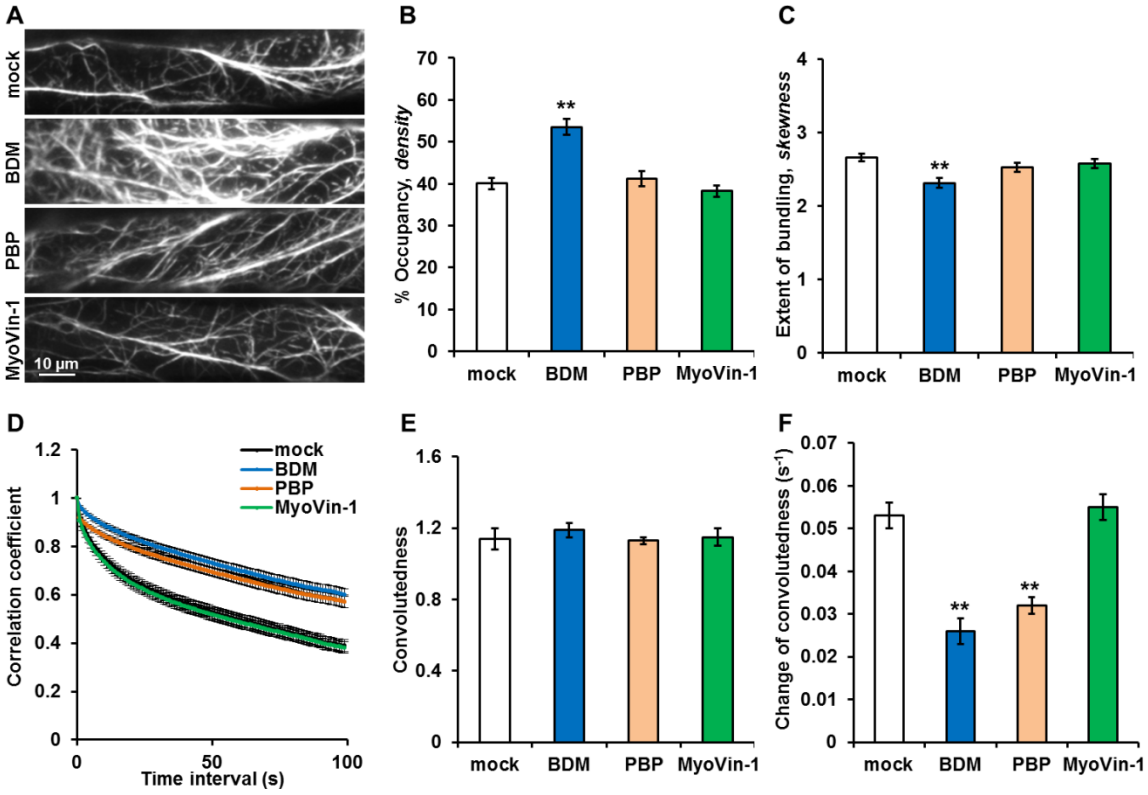

Figure 3.3. Myosin inhibitors reduce actin dynamics.

Figure 3.3. Myosin inhibitors reduce actin dynamics.

(A) Representative images of epidermal cells from 5-d-old etiolated hypocotyls expressing GFP-fABD2 treated for 15 min with mock (0.2% DMSO), 30 mM BDM, 10 µM PBP, or 20 µM MyoVin-1 prior to imaging. VAEM images were collected from the basal region of the hypocotyl. Bar = 10 µm.

(B) and (C) Quantitative analyses of the architecture of actin arrays in drug-treated epidermal cells. (B) Percentage of occupancy (*density*) was measured. Filament density was significantly increased in BDM-treated cells compared to mock treatment, whereas PBP and MyoVin-1 had no effect. Values given are means ± SE (n ≥ 100 images from 20 seedlings per treatment; *t* test: **P < 0.01). (C) The extent of filament bundling (*skewness*) was measured. Bundling was slightly decreased in BDM-treated cells compared to mock treatment. The same images used for (B) were analyzed for bundling (*t* test: **P < 0.01).

(D) Pairwise correlation coefficient was calculated at all possible temporal spacings from time-lapse series of epidermal cells in the basal region of the hypocotyl. Filaments in BDM- and PBP-treated cells had significantly reduced overall actin dynamicity compared to mock treatment, whereas MyoVin-1 had no effect. Values given are means ± SE (n ≥ 35 cells from 20 seedlings per treatment; analysis of variance, P < 0.01).

(E) and (F) Quantitative analyses of single actin filament shape change in drug-treated epidermal cells. (E) Convolutedness showed no significant difference in all myosin inhibitor-treated cells compared to mock treatment. (F) Rate of change of convolutedness was significantly decreased in cells treated with BDM and PBP compared to mock treatment. The same images used for (D) were analyzed for filament shape change. Values given are means ± SE (n ≥ 50 filaments from 10 seedlings per treatment; *t* test: **P < 0.01).

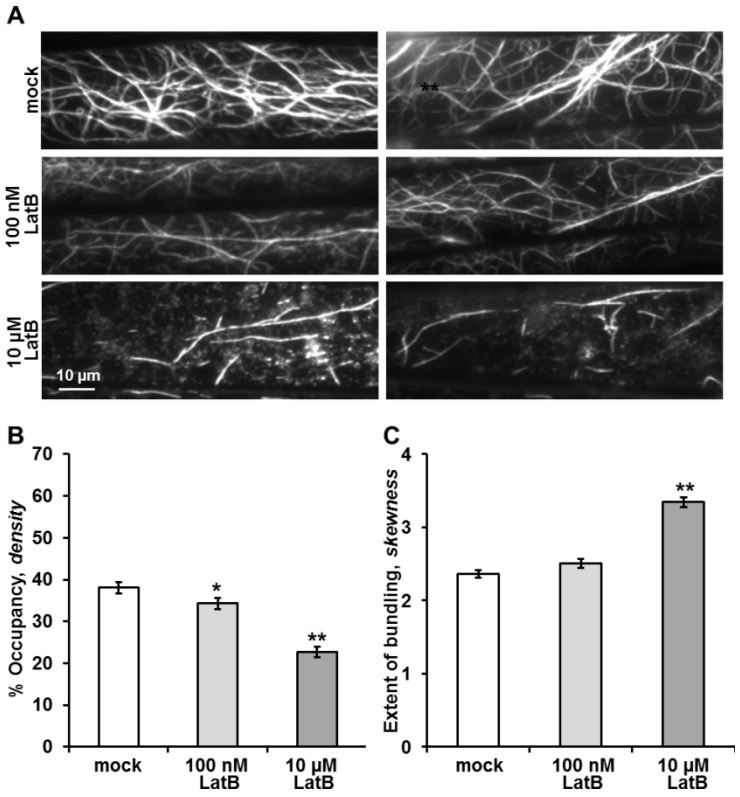

Figure 3.4. LatB treatment disrupts cortical actin arrays.

(A) Representative images of epidermal cells from 5-d-old etiolated hypocotyls expressing GFP-fABD2 treated for 15 min with mock (0.2% DMSO), 100 nM LatB, 10 µM or LatB prior to imaging. VAEM images were collected from the basal region of the hypocotyl. Bar = 10 µm.

(B) and (C) Quantitative analyses of the architecture of actin arrays in drug-treated epidermal cells. (B) Percentage of occupancy (*density*) was measured. Filament density was significantly reduced in LatB-treated cells compared to mock treatment. Values given are means ± SE (n ≥ 100 images from 20 seedlings per treatment; *t* test: *P < 0.05, **P < 0.01). (C) The extent of filament bundling (*skewness*) was measured. Bundling was increased in cells treated with 10 µM LatB compared to mock treatment. The same images used for (B) were analyzed for bundling (*t* test: **P < 0.01).

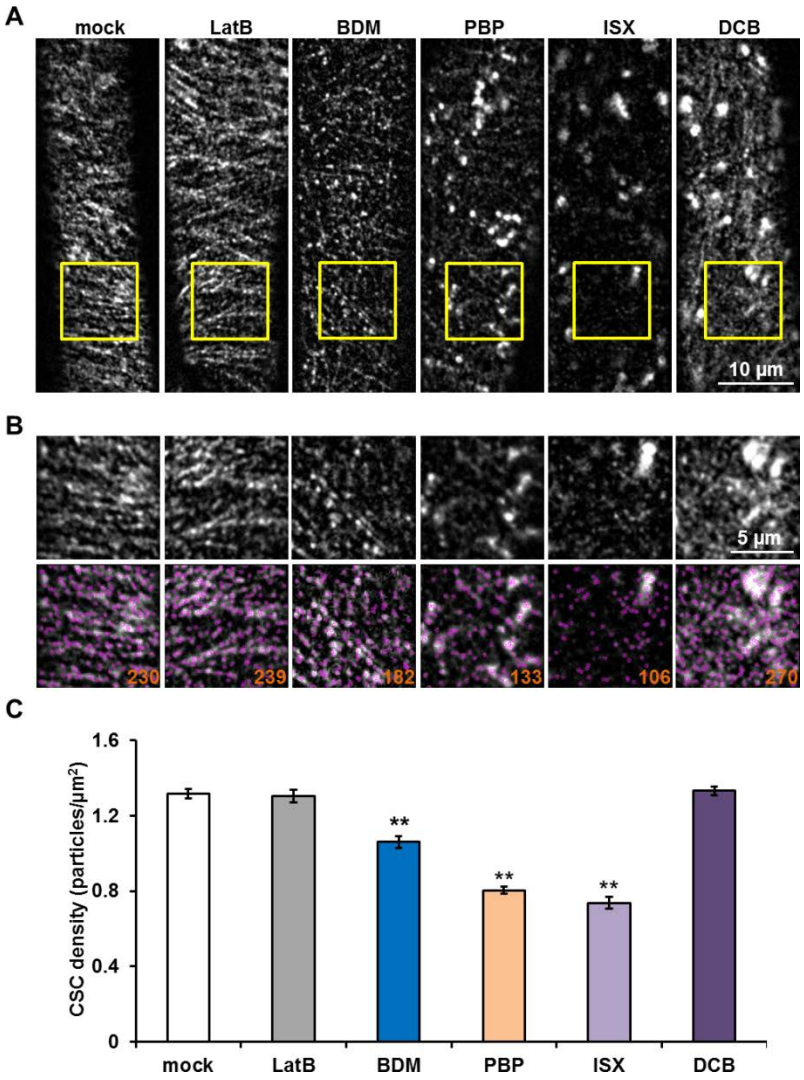

Figure 3.5. The density of CSC particles at the PM is reduced after treatment with myosin inhibitors.

(A) Representative time projections of plasma membrane (PM)-localized YFP tagged cellulose synthase 6 (YFP-CESA6) particles showing the distribution of cellulose synthase complex (CSC) in hypocotyl epidermal cells. Hypocotyls were treated for 15 min with mock (0.2% DMSO), 10 µM LatB, 30 mM BDM, 10 µM PBP, 100 nM isoxaben (ISX), or 5 µM 2,6-dichlorobenzonitrile (DCB) prior to imaging. Time-lapse series were collected with spinning-disk confocal microscopy from epidermal cells at the apical region of 3-d-old hypocotyls using 5-s intervals for 5 frames. Time projections were generated with average intensity for all 5 images. Bar = 10 µm. (B) Magnified ROIs (yellow box in A) with CSC particles detected using "TrackMate" plugin from ImageJ (marked in purple). The number of particles in each ROI is given in orange. Bar = 5 µm. (C) Quantitative analysis of CSC density in inhibitor-treated epidermal cells. The CSC density was significantly decreased after BDM, PBP, and ISX treatments, but not with LatB and DCB treatments. Values given are means ± SE (n > 20 cells per treatment; Student's t test, **P < 0.01).

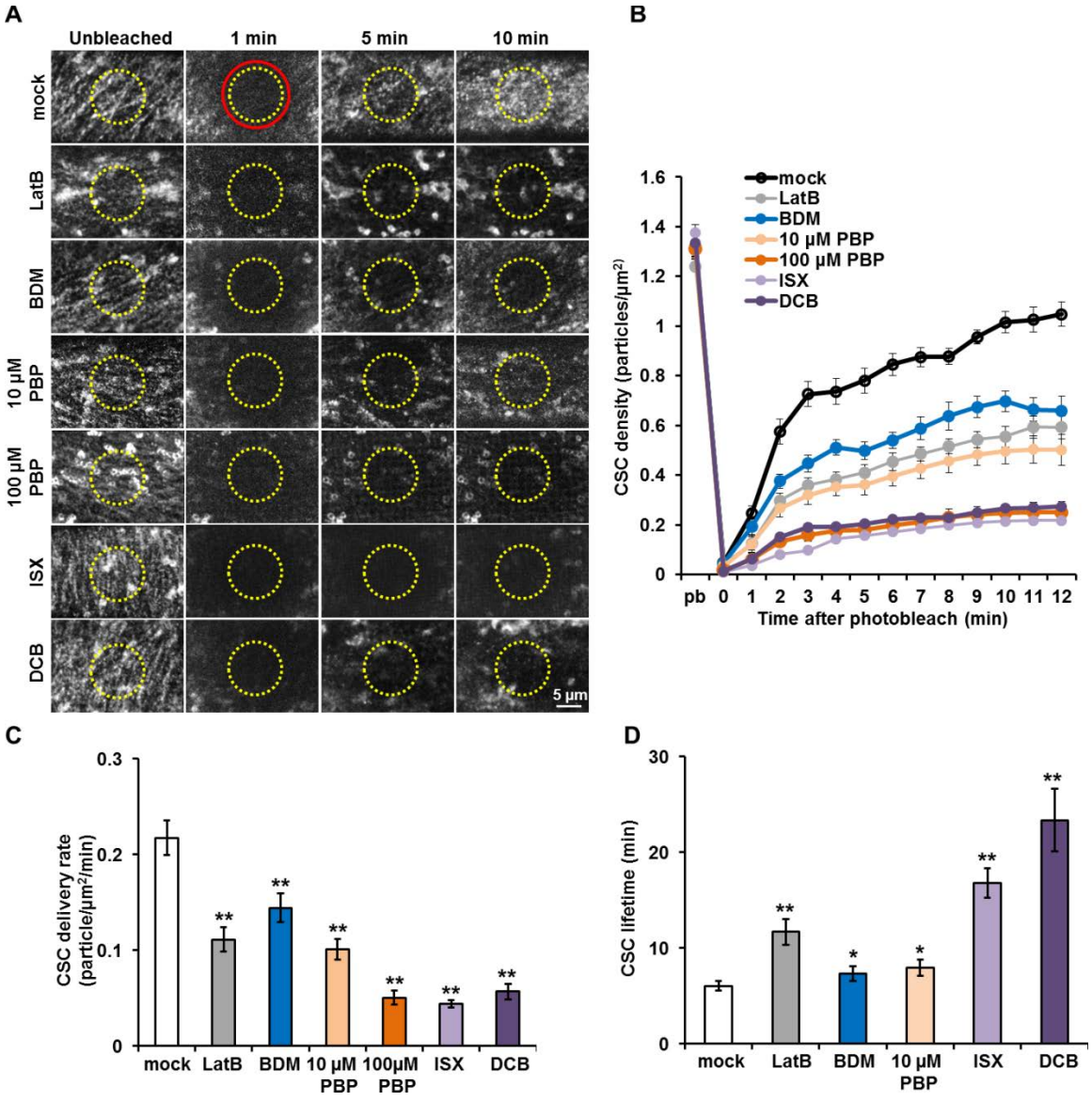

Figure 3.6. Delivery of CSC to the PM is inhibited by myosin inhibitors.

Figure 3.6. Delivery of CSC to the PM is inhibited by myosin inhibitors.
(A) Representative time projections of PM-localized CSC particle recovery after photobleaching following treatment with mock (0.2% DMSO), 10 µM LatB, 30 mM BDM, 10 µM PBP, 100 µM PBP, 100 nM ISX, or 5 µM DCB. Three-d-old hypocotyls were mounted in inhibitor and time-lapse series were collected from epidermal cells by spinning-disk confocal microscopy with 5-s intervals for 150 frames. One region (circle in red solid line) was photobleached using 100% laser power with the 515-nm laser line after the 6^{th} frame. Time projections were generated with average intensity for the last 5 images from each minute. CSC particles were measured within the region of interest (ROI, circle in yellow dashed line). Bar = 5 µm. (B) Quantitative analysis of CSC density before and after photobleaching. Values given are means ± SE (n = 10 ROIs per treatment). (C) The delivery rate of CSC to the PM was calculated as the slope of linear regression from the CSC density within each ROI during the initial 3 min of recovery. Values given are means ± SE (n = 10 ROIs per treatment; Student's t test,*P<0.05, **P < 0.01). (D) Lifetime of CSC at the PM was calculated using the delivery rate in (C) divided by CSC density in Figure 3.5C. The CSC delivery rate was significantly reduced, and the apparent lifetime was increased after treatment with LatB, BDM, PBP, ISX, and DCB.

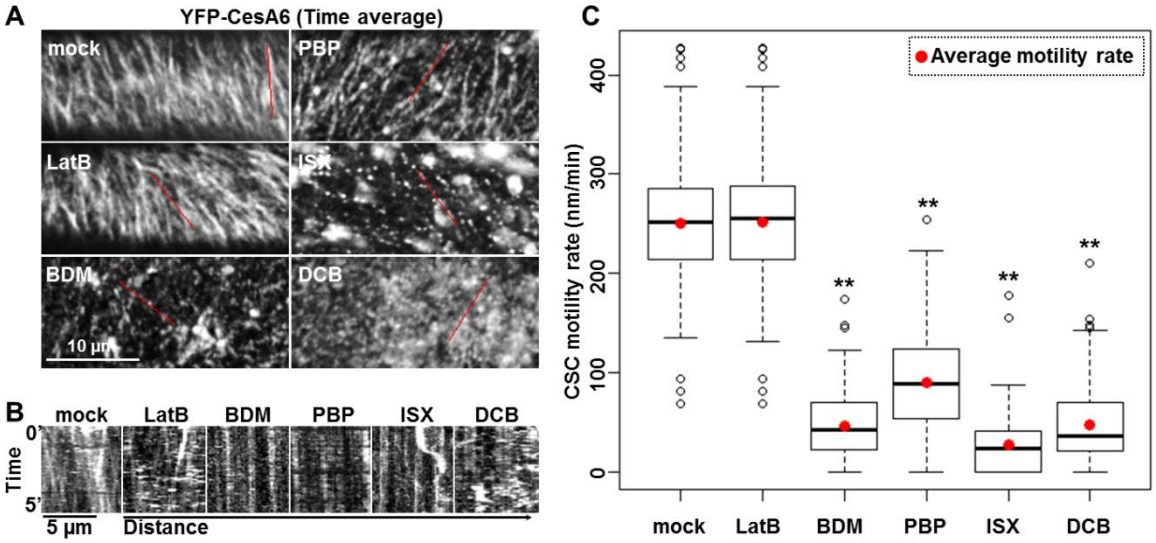

Figure 3.7. The motility of CSC at the PM is reduced by myosin inhibitors.

(A) Representative time projections of the trajectories of CSC particles at the PM following 15 min treatment with mock (0.2% DMSO), 10 µM LatB, 30 mM BDM, 10 µM PBP, 100 nM ISX, or 5 µM DCB. Time-lapse series of epidermal cells from the apex of 3-d-old hypocotyls were collected by spinning-disk confocal microscopy using 5-s intervals for 61 frames. Time projections were generated with average intensity of all 61 images. Bar = 10 µm. (B) Kymographs of selected trajectories (red lines) in (A). Bar = 5 µm. (C) Box-whisker plots show the motility rate of CSC measured by kymograph after drug treatments. The body of the box consists of median, the first and third quartiles. Whiskers represent 1.5 times of inter-quartile range (IQR) above or below the first and third quartiles, respectively. Black empty circles represent outliers off the range of whiskers. Red solid circles show the average CSC motility rate. Quantitative analyses show that BDM, PBP, ISX, and DCB treatment significantly reduced the motility of CSC at the PM (n > 500 CSC particles per treatment, Student's t test, **P<0.01).

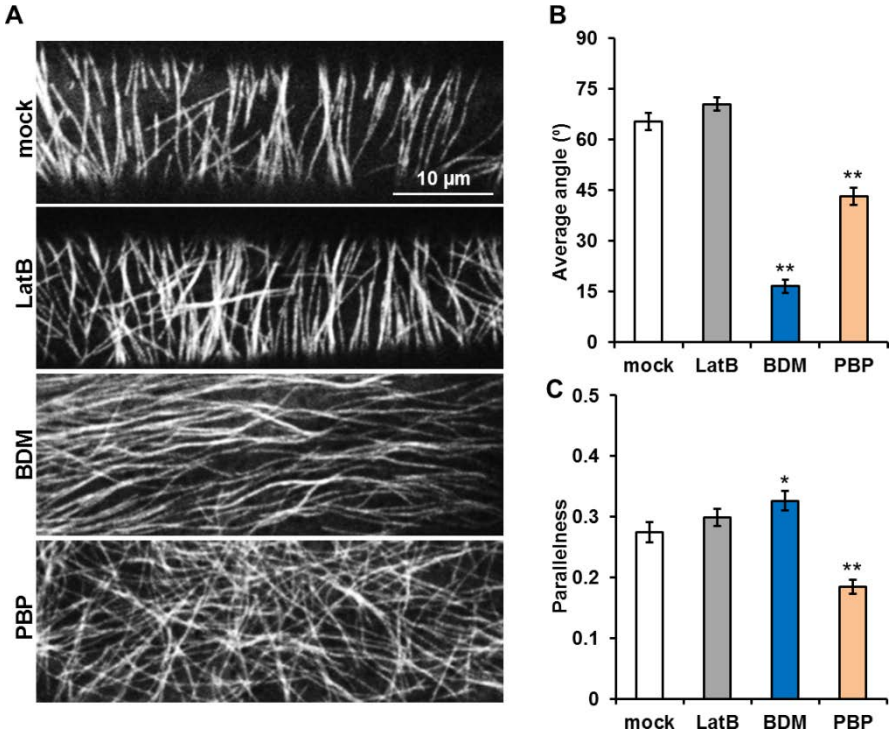

Figure 3.8. Myosin inhibitors induce the reorientation of cortical microtubules.
(A) Representative images of epidermal cells from 3-d-old etiolated hypocotyls expressing YFP-tagged β-tubulin5 (YFP-TUB5). Hypocotyls were treated for 15 min with mock (0.2% DMSO), 100 nM LatB, 30 mM BDM, or 10 µM PBP prior to imaging. Images were collected with spinning-disk confocal microscopy at the apical region of 3-d-old hypocotyls. Bar = 10 µm. (B and C) Quantitative analyses of the orientation of cortical microtubule arrays. (B) Average angle of microtubules with respect to the longitudinal axis of epidermal cells was measured. Angle was significantly decreased upon BDM and PBP treatment. (C) The parallelness of microtubules with respect to each other was measured. Parallelness was significantly reduced after PBP treatment, whereas BDM modestly, but significantly increased parallelness of microtubules. Values given are means ± SE (n > 100 cells, Student's t test, *P < 0.05, **P < 0.01).

CHAPTER 4. DISCUSSION

4.1 Summary of results

In this study, we dissected the role of plant myosin in cell wall assembly, including cellulose deposition as well as the distribution and dynamic behavior of cellulose synthase complexes (CSCs). Biochemical determination of cellulose content showed that the amount of crystalline cellulose was significantly decreased in a *myosin xi* triple knockout mutant (*xi3KO*). In order to test the function of myosin in regulating CSC distribution and dynamic behavior, we identified pentabromopseudilin (PBP) as a potential plant myosin inhibitor. Short-term treatment with PBP reduced the rate of Golgi motility as well as overall actin dynamicity, which are myosin-dependent processes. Combining a pharmacological approach with high resolution live-cell imaging, we found that CSC density at the plasma membrane (PM) was reduced when plant myosin activity was inhibited with PBP and BDM treatments. This reduction of CSC density could be due to a disruption of the balance between delivery and internalization of CSC at the PM. Inhibiting actin polymerization and myosin activity caused a reduced CSC delivery rate and an increased CSC lifetime at the PM. Surprisingly, we found that myosin influences CSC motility in an actin-independent manner, as PBP treatment inhibits the motility of CSC at the PM, whereas disrupting actin organization does not. Finally, inhibiting myosin

activity also altered cortical microtubule orientation, which could potentially be related to the inhibition of CSC motility, or could represent a form of actin-microtubule crosstalk.

4.2 Validation of PBP as a myosin inhibitor for use in plants

Inhibitors of myosin have been widely used to study myosin function. In plants, N-ethylmaleimide (NEM), ML-7, and 2,3-butanedione monoxime (BDM) have been widely used to test myosin function. There are advantages as well as potential risks associated with use of these drugs as myosin inhibitors in plants.

NEM is a sulfhydryl group crosslinker, which potentially inhibits the activity of many different proteins, including myosins. Myosin protein crosslinked with NEM shows no motor activity, but can still bind to actin filaments (Sekine et al., 1962). One problem with NEM is its poor specificity, especially for in vivo experiments. In biology studies, NEM is often used as an irreversible inhibitor to modify cysteine residues at the active site of proteins (Gregory, 1955), thus this reaction is not specific to myosin. Actually, NEM has been found to inhibit multiple cellular processes in plants. For example, NEM inhibits the auxin-stimulated NADH oxidase activity in soybean (Morré et al., 1995), and also inactivates plasma membrane H^+-ATPase in oats (Katz & Sussman, 1987). Thus, results using NEM on plant cells to inhibit myosin-based functions, for example chloroplast motility in *Vallisneria* mesophyll cells (Liebe & Menzel, 1995), should be interpreted with caution.

ML-7 has been characterized as an inhibitor of smooth muscle myosin light chain kinase (MLCK), which blocks the phosphorylation of myosin light chain (MLC), thereby

inhibiting the activity of smooth muscle myosin II (Saitoh et al., 1987). Treatment of plant cells with ML-7 blocked cytoplasmic streaming in *Tradescantia* stamen hair cells (Molchan et al., 2002), and inhibited chloroplast accumulation in *Arabidopsi*s leaf cells (Paves & Truve, 2007); however, any conclusions about plant myosin function drawn from ML-7 treatment are rather questionable. First, the inhibitory effect of ML-7 is not specific to MLCK, even in animal cells. Although ML-7 has better selectivity than its precursor ML-9, it still shows inhibition of mitogen- and stress-activated protein kinase 1 (MSK1) (Bain et al., 2003, Saitoh et al., 1987). Second, there are no genes characterized as MLC in the *Arabidopsis* genome, and consequently, no MLCK genes or proteins have been identified. However, functional analysis of plant myosin sequences show that plant myosin contains multiple IQ motifs, which serve as potential binding sites for light chains (Syamaladevi et al., 2012). Also, it was reported that actomyosin-dependent vesicle transport in *Chara* can be regulated by calcium signaling and phosphorylation (Morimatsu et al., 2002, McCurdy & Harmon, 1992). The detection of calmodulin (CaM) in myosin extracts from lily pollen tubes and tobacco Bright Yellow 2 (BY-2) cells has been used to suggest that CaM might be a MLC in plants (Yamamoto et al., 1999, Yokota et al., 1999b, Yokota et al., 1999a). Thus, the potential effectiveness of ML-7 in inhibiting myosin-related cellular processes should not be ruled out, but the specificity of the drug can only be tested after the real target is identified.

Butanedione monoxime (BDM) was originally found to inhibit the contraction of cardiac muscle (Bergey et al., 1981, Li et al., 1985), and later, characterized as a non-competitive inhibitor of skeletal myosin II ATPase, by stabilizing the $M{\cdot}ADP{\cdot}P_i$ intermediate

(Herrmann et al., 1992, McKillop et al., 1994). The effectiveness of BDM on plant myosin XI has been demonstrated through in vitro biochemical studies. The in vitro motility of myosin proteins isolated from *Chara* or lily pollen tubes is inhibited by BDM treatment (Funaki et al., 2004, Tominaga et al., 2000). Also, treatment with BDM inhibits organelle motility and actin dynamicity, which are consistent with results from *myosin xi* mutants (Nebenführ et al., 1999, Peremyslov et al., 2010, Ueda et al., 2010, Staiger et al., 2009, Cai et al., 2014). BDM has been used as a general myosin inhibitor due to its inhibition of non-muscle myosin II and myosin V (Cramer & Mitchison, 1995), and is currently considered as the best characterized plant myosin inhibitor. However, BDM has relatively low affinity for the myosin ATPase domain, and has to be applied in tens of millimolar concentration to be effective (Funaki et al., 2004). In animal cells, BDM affects serine/threonine protein phosphorylation (Stapleton et al., 1998), which raises the problem of off-target inhibition in plant cells.

In this study, we tested two myosin V inhibitors, pentabromopseudilin (PBP) and myosin V inhibitor-1 (MyoVin-1), as potential plant myosin inhibitors. We found that PBP, at micromolar concentration, could inhibit myosin-dependent Golgi motility and actin dynamicity similar to BDM, whereas MyoVin-1 showed no difference compared to mock treatment, indicating that PBP may be used as a new myosin inhibitor in plants. Further studies using an *Arabidopsis* line expressing YFP-tagged myosin XI-K (YFP-XI-K) that complements the *xi3KO* mutant showed that PBP inhibits the motility of YFP-XI-K in a dose-dependent manner (Weiwei Zhang, personal communication), confirming that PBP

targets plant myosin. Ultimately, however, PBP should be tested for the ability to inhibit biochemically the actin-activated ATPase or in vitro motility of purified plant myosins.

4.3 Myosin XI is involved in cellulose deposition

It has been hypothesized for decades that plant myosin is involved in cell wall deposition (Nebenführ et al., 1999), yet no direct evidence supports this hypothesis under normal physiological conditions. During the formation of cell wall appositions or papillae in response to fungal penetration of host plant cells, inhibition of myosin activity using drugs (NEM and BDM) or a myosin mutant inhibits the deposition of callose and lignin-like wall polymers (Yang et al., 2014). Moreover, disrupting actin organization with cytochalasin D results in a decrease in α-cellulose and matrix polysaccharide deposition in tobacco protoplasts (Leucci et al., 2007).

Currently, evidence indicating that plant myosin is involved in cellulose deposition is only circumstantial. First, plant myosin XI has been shown to regulate the growth and size of cells and organs. Knocking out *myosin xi* genes showed a dwarf phenotype in *Arabidopsis* (Prokhnevsky et al., 2008, Peremyslov et al., 2010). The severity of the phenotype directly correlated with the number of *myosin xi* genes that were knocked out. Also, it was shown that the activity of myosin ATPase correlated with the size of plant cells and organs. Swapping the head domain of *Arabidopsis* Myosin XI-2 with faster or slower motor domains caused plant cells and organs to be larger or smaller, respectively (Tominaga et al., 2013). These results indicate that plant myosin XI may serve as the motor to deliver cell wall-related material to the PM. Second, as the tracks

that myosins move along, actin filaments are reported to be involved in cellulose deposition (Sampathkumar et al., 2013). For example, disrupting proper actin organization with latrunculin B (Lat B) or an *act2 act7* double mutant causes a reduction of crystalline cellulose content in *Arabidopsis*. Further investigation indicates that actin facilitated the delivery and internalization of CSC at the PM (Sampathkumar et al., 2013). Disrupting actin organization causes no change in CSC density at the PM, but a reduction of delivery rate, thus implying an inhibition of internalization. With the determination of cellulose content in etiolated *Arabidopsis* hypocotyls using biochemical analysis, we found that seedlings grown on medium containing 100 nM LatB had a decreased cellulose content, which is consistent with the findings in Sampathkumar et al., 2013. Moreover, we found that the cellulose content in the *myosin xi3KO* mutant (Peremyslov et al., 2010, Cai et al., 2014) was also significantly reduced. This result, for the first time, provides direct evidence that plant myosin is involved in cellulose deposition.

4.4 Plant myosin regulates the distribution of CSC by participating in the delivery of CSC to the PM

To be a functional unit that synthesizes cellulose microfibrils, the assembled CSC has to be secreted to the PM. There are at least two routes for the delivery of CSC, one is directly from a pausing CSC-containing Golgi (Crowell et al., 2009), the other, which is probably the major route, is through SmaCC/MASC, which helps CSC recycle back to the PM through a CSI1-facilitated pathway (Gutierrez et al., 2009, Sampathkumar et al., 2013, Lei et al., 2015). However, disrupting cortical microtubules does not alter CSC

delivery (Gutierrez et al., 2009). There is evidence supporting that both actin and myosin are involved in the delivery of CSC into the PM. The motility of secretory vesicles labeled with SCAMP2 was reduced in a *myosin xi* mutant, suggesting that plant myosin XI is involved in a general secretory pathway (Peremyslov et al., 2012). Also, steady-state level of Penetration 1 protein (PEN1) at the PM was inhibited in *myosin xi* mutant or upon treatment with myosin inhibitors (Yang et al., 2014). Recent studies on a myosin XI receptor protein, MyoB, support a model that myosin-dependent, MyoB-mediated trafficking of a specialized vesicle drives motility of organelles and vesicles through cytoplasmic streaming (Peremyslov et al., 2015, Peremyslov et al., 2013). Also, it has been recently found that the exocytosis of CESA requires the proper function of TGN/EE (Luo et al., 2015), whose motility is myosin dependent (Avisar et al., 2012).

Multiple studies show that actin filaments are involved in the trafficking of CSC in plant cells. Disrupting actin organization with cytochalasin D or LatB reduces the motility of CESA-containing Golgi, and causes the clustering of Golgi and uneven distribution of CSC at the PM (Crowell et al., 2009, Gutierrez et al., 2009, Sampathkumar et al., 2013). Upon treatment with the actin stabilizing drug, jasplakinolide, CESA-containing Golgi follows a "disorganized trajectory" (Sampathkumar et al., 2013). The motility of distinct populations of SmaCC/MASC was found to be dependent on both microtubules and actin filaments. Cortical microtubules guide orientation of SmaCC/MASC motility, and microtubule depolymerization is thought to be the driving force for the motility of cortical SmaCC/MASCs (Crowell et al., 2009, Gutierrez et al., 2009). However, a subpopulation of subcortical SmaCC/MASCs are found to move along actin filaments

(Sampathkumar et al., 2013). Disrupting actin inhibits the movement of subcortical SmaCC/MASCs and causes an increase in the number of cortical SmaCC/MASCs, suggesting that there is an interchange of SmaCC/MASCs between actin filaments and microtubules (Sampathkumar et al., 2013). Thus, it has been hypothesized that Golgi-derived SmaCC/MASCs move along actin filaments, and pause on cortical microtubules during the insertion of CSC into the PM (Li et al., 2015, Wallace & Somerville, 2014). Our data showed a significant decrease in CSC delivery at the PM with no change in density upon treatment with LatB, which is consistent with the results of Sampathkumar et al., 2013. Moreover, we found that treatment with myosin inhibitors reduced not only the delivery of CSC, but also the density of CSC at the PM.

To maintain the proper amount of CSC at the PM, existing CSC has to be internalized. However, due to the high density of CSCs at the PM, and the limits of fluorescent microscopy, at present, there is no tool to directly measure the internalization rate of CSC from the PM. A parameter, “CSC lifetime”, which is calculated as CSC density divided by delivery rate, was applied to infer the rate of CSC internalization. Due to the fact that disrupting actin filaments causes a decrease of CSC delivery rate, but no change in density, it was inferred that lifetime of CSC at the PM was extended (Sampathkumar et al., 2013), suggesting that actin filaments are necessary for the internalization of CSC. It was found that clathrin-mediated endocytosis played at least a partial role in the internalization of CSC. In the Arabidopsis *μ2* and *twd40-2* mutants, which are deficient in clathrin-mediated endocytosis, an increase in PM-localized CSC density with no change in the rate of delivery is observed (Bashline et al., 2013, Bashline et al., 2015). Evidence

on whether actin filaments facilitate or inhibit endocytosis is controversial (Baisa et al., 2013). It has been shown that the lifetime of clathrin-coated pits was extended by the treatment of LatB (Konopka & Bednarek, 2008). In addition, treatment with LatB inhibits the internalization of a membrane-localized receptor, Flagellin-sensitive 2 (FLS2) (Beck et al., 2012). However, accumulation of actin filaments inhibits auxin-induced PIN1 internalization, suggesting that actin filaments may block endocytosis (Nagawa et al., 2012). Plant myosin has been found to be implicated in clathrin-mediated endocytosis. Inhibiting myosin with BDM inhibits the endocytosis of FLS2 (Beck et al., 2012). Using the calculation from CSC density and delivery rate, we found that CSC lifetime at the PM was significantly increased by treatment with myosin inhibitors, suggesting that myosin is necessary for CSC internalization. Interestingly, compared to LatB treatment, which showed no significant change in CSC density, the treatment with myosin inhibitors induced a stronger inhibition of delivery, but a weaker effect on internalization. This could probably break the equilibrium between delivery and internalization, thus reducing the density of CSC at the PM (Figure 4.1). In other words, myosin may play a greater role in delivery compared to internalization of CESA in plant epidermal cells, whereas actin is postulated to participate equally in both.

4.5 Plant myosin is involved in CSC motility and microtubule orientation by an unknown mechanism

The motility of CSC is guided by cortical microtubules and thought to be driven by the synthesis of cellulose (McFarlane et al., 2014, Bashline et al., 2014, Wallace & Somerville,

2014). Both our study and published results from other groups showed that disrupting actin organization does not alter the rate of CSC motility (Sampathkumar et al., 2013). Similarly, we found that doses of LatB that have pronounced effects on actin dynamics and organization have no effect on CSC motility. Surprisingly, we found that the motility of CSC was significantly inhibited by short-term treatment with myosin inhibitors, which indicates that plant myosin could possibly influence CSC motility in an actin-independent manner. However, the mechanism by which myosin is involved in regulating CSC motility is not known. Several factors have been proposed to regulate the motility rate of CSC, which is thought to be mostly correlated with the rate of cellulose synthesis (Bashline et al., 2014, McFarlane et al., 2014). The most direct factor that can affect CSC motility is the amount of UDP-glucose available for cellulose synthesis. It was assumed that sucrose synthase (SuS) associates with CSC to provide a local supply of UDP-glucose (Amor et al., 1995, Fujii et al., 2010). The existence of GPI-anchored proteins that are required for normal cellulose synthesis, like COBRA and SOS5, might also regulate CSC motility (Harpaz-Saad et al., 2011, Roudier et al., 2005, Schindelman et al., 2001). Plant myosin could potentially regulate the localization of these CSC associated/regulating proteins through the secretory pathway.

Another possible way to regulate CSC motility is through components of CSC other than CESA proteins. Cellulose synthase interactive1 (CSI1) and Korrigan1 (KOR1) were both identified as components of CSC to maintain its normal function (McFarlane et al., 2014). Recent studies on the *csi1* mutant, which knocked out the crosslinker for CSC and microtubule, show a lowered CSC motility rate as well as change in microtubule

orientation (Li et al., 2012, Bringmann et al., 2012). A similar situation with decreased CSC motility and altered microtubule orientation is also observed in the *kor1* mutant (Paredez et al., 2008, Vain et al., 2014). Thus, it is possible that plant myosin facilitates the interaction between CESAs and CSI1/KOR1, the delivery of components to the PM, or both.

The possibility that plant myosin coordinates the interaction among components of CSC can also explain the observation that microtubule orientation is altered with the treatment of myosin inhibitors. In addition to disrupting CSI1 or KOR1 genetically, it was found that altering CSC activity induced changes in microtubule orientation (Paredez et al., 2008, Fujita et al., 2013), which suggests a potential feedback loop between CSC and cortical microtubules. In addition, our data showed that PBP was less effective than BDM in inhibiting both CSC motility and microtubule orientation, suggesting that the microtubule reorientation induced by myosin inhibitors may correlate with the inhibition of CSC motility.

Even though LatB treatment did not alter microtubule orientation, it is still possible the myosin affects microtubule orientation through actin. The dynamic interaction of cortical microtubules and actin filaments has been quantitatively described by visualization of fluorescently-tagged microtubule and actin reporters (Sampathkumar & Wightman, 2015, Sampathkumar et al., 2011). Our data showed that treatment with myosin inhibitors significantly inhibited the dynamic change of actin filament (Cai et al., 2014), which could have a potential influence in regulating microtubule orientation with a mechanism that is different from LatB-induced actin change. Granted, we cannot rule

out the possibility that the microtubule reorientation observed in our experiments is still actin-dependent, due to the fact that the concentration and duration of LatB we applied was not enough to destroy all actin filaments and bundles in epidermal cells. Thus, it is possible that myosin regulates microtubule orientation through actin bundles.

4.6 Overall significance of findings in this study

In order to dissect the function of plant myosin in regulating cellulose deposition and CSC behavior, we identified PBP as a potential new plant myosin inhibitor, which is effective at micromolar concentrations. With biochemical determination of cellulose content in the *xi3KO* mutant, we provided the first direct evidence that plant myosin XI is involved in the deposition of cellulose. Characterization of CSC behavior revealed that the density of CSC was reduced upon treatment with myosin inhibitors, which is probably due to the differential inhibition of CSC delivery and internalization. Surprisingly, inhibition of myosin caused a significant reduction in the rate of CSC motility as well as altered microtubule orientation, which are not consistent with LatB treatment, suggesting that these changes are potentially independent from actin filaments, thus, uncovering a unique facet of myosin function.

4.7 Future perspectives

There are several things that could be considered in the future to strengthen and extend this study. First, further characterization of PBP as a plant myosin inhibitor could be evaluated with direct in vitro biochemical measurement of ATPase activity of

Arabidopsis Myosin XI proteins. This experiment could provide direct evidence about the target of PBP. Second, the involvement of plant myosin in cell wall deposition could be backed-up by the analysis of cell wall components using seedlings grown on medium containing myosin inhibitors. Further analysis on carbohydrates linkage could potentially reveal exactly which polysaccharide molecule is delivered through a myosin-dependent pathway. Third, the CSC behavior could be observed in *myosin xi* mutants to eliminate the possible unspecific effect of inhibitors. Fourth, the rate of CSC internalization can be observed directly with CESA tagged with photo-activatable fluorescent protein, thus the endocytosis of CSC can be directly evaluated. Fifth, the mechanism of how myosin regulates CSC motility and microtubule orientation should addressed, potentially by looking at the interactive relationship between CSC and CSI1 or KOR1.

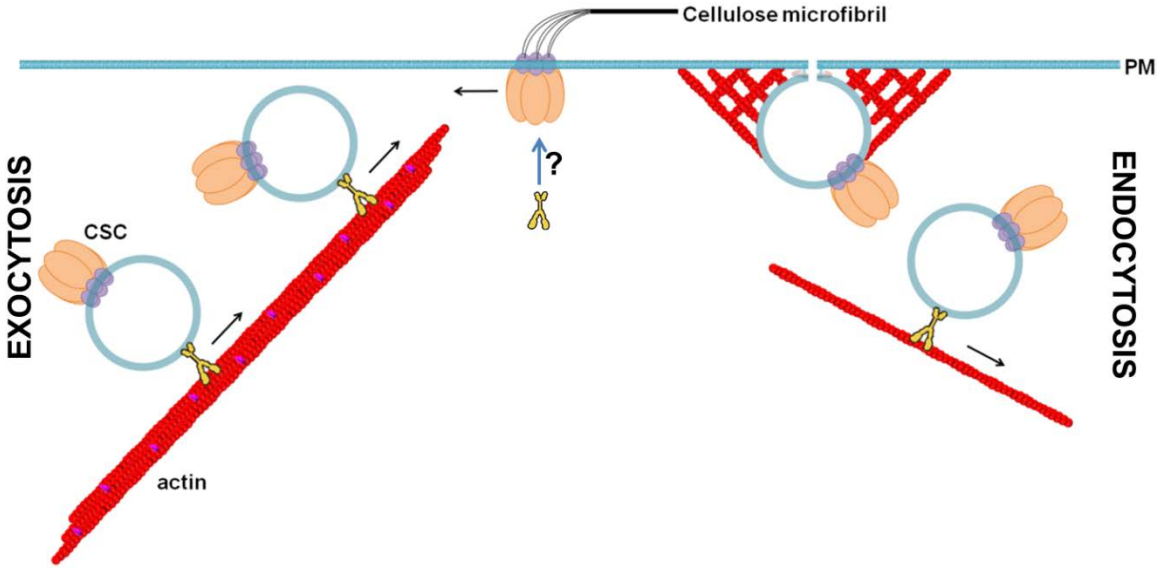

Figure 4.1. A model for how myosin regulates CSC behavior.
Treatment of epidermal cells with myosin inhibitors caused a reduced rate of delivery and extended lifetime of CSC at PM, which is similar to that reported for actin-disrupted cells (Sampathkumar et al., 2013). These results suggest that plant myosins may work with actin filaments to promote the delivery and internalization of CSC. Moreover, myosin may play a greater role in delivery compared to internalization, based on the observed decrease of CSC density after treatment with myosin inhibitors. But, the lifetime measurement suggests that exocytosis and endocytosis may be almost equally impacted by BDM and PBP. Also, myosin could regulate the motility of CSC, independent of actin, by an unknown mechanism.

LIST OF REFERENCES

LIST OF REFERENCES

Akkerman M, Overdijk EJ, Schel JH, Emons AMC, Ketelaar T, 2011. Golgi body motility in the plant cell cortex correlates with actin cytoskeleton organization. *Plant Cell Physiol* **52**, 1844-55.

Amor Y, Haigler CH, Johnson S, Wainscott M, Delmer DP, 1995. A membrane-associated form of sucrose synthase and its potential role in synthesis of cellulose and callose in plants. *Proc Natl Acad Sci USA* **92**, 9353-7.

Arioli T, Peng L, Betzner AS*, et al.*, 1998. Molecular analysis of cellulose biosynthesis in *Arabidopsis*. *Science* **279**, 717-20.

Avisar D, Abu-Abied M, Belausov E, Sadot E, 2012. Myosin XIK is a major player in cytoplasm dynamics and is regulated by two amino acids in its tail. *J Exp Bot* **63**, 241-9.

Avisar D, Abu-Abied M, Belausov E, Sadot E, Hawes C, Sparkes IA, 2009. A comparative study of the involvement of 17 *Arabidopsis* myosin family members on the motility of Golgi and other organelles. *Plant Physiol* **150**, 700-9.

Avisar D, Prokhnevsky AI, Makarova KS, Koonin EV, Dolja VV, 2008. Myosin XI-K is required for rapid trafficking of Golgi stacks, peroxisomes, and mitochondria in leaf cells of *Nicotiana benthamiana*. *Plant Physiol* **146**, 1098-108.

Bain J, Mclauchlan H, Elliott M, Cohen P, 2003. The specificities of protein kinase inhibitors: an update. *Biochem J* **371**, 199-204.

Baisa GA, Mayers JR, Bednarek SY, 2013. Budding and braking news about clathrin-mediated endocytosis. *Curr Opin Plant Biol* **16**, 718-25.

Bashline L, Lei L, Li S, Gu Y, 2014. Cell wall, cytoskeleton, and cell expansion in higher plants. *Mol Plant* **7**, 586-600.

Bashline L, Li S, Anderson CT, Lei L, Gu Y, 2013. The endocytosis of cellulose synthase in *Arabidopsis* is dependent on μ2, a clathrin-mediated endocytosis adaptin. *Plant Physiol* **163**, 150-60.

Bashline L, Li S, Zhu X, Gu Y, 2015. The TWD40-2 protein and the AP2 complex cooperate in the clathrin-mediated endocytosis of cellulose synthase to regulate cellulose biosynthesis. *Proc Natl Acad Sci USA* **112**, 12870-5.

Beck M, Zhou J, Faulkner C, Maclean D, Robatzek S, 2012. Spatio-temporal cellular dynamics of the *Arabidopsis* flagellin receptor reveal activation status-dependent endosomal sorting. *Plant Cell* **24**, 4205-19.

Bergey JL, Reiser J, Wiggins JR, Freeman AR, 1981. Oximes:'Enzymatic'slow channel antagonists in canine cardiac purkinje fibers? *Eur J Pharmacol* **71**, 307-19.

Bowling A, Brown Jr R, 2008. The cytoplasmic domain of the cellulose-synthesizing complex in vascular plants. *Protoplasma* **233**, 115-27.

Bringmann M, Li E, Sampathkumar A, Kocabek T, Hauser M-T, Persson S, 2012. POM-POM2/cellulose synthase interacting1 is essential for the functional association of cellulose synthase and microtubules in *Arabidopsis*. *Plant Cell* **24**, 163-77.

Cai C, Henty-Ridilla JL, Szymanski DB, Staiger CJ, 2014. *Arabidopsis* myosin XI: a motor rules the tracks. *Plant Physiol* **166**, 1359-70.

Carpita NC, 2011. Update on mechanisms of plant cell wall biosynthesis: how plants make cellulose and other (1→ 4)-β-D-glycans. *Plant Physiol* **155**, 171-84.

Carpita NC, Shea EM, 1989. Linkage structure of carbohydrates by gas chromatography-mass spectrometry (GC-MS) of partially methylated alditol acetates. In. *Analysis of Carbohydrates by GLC and MS.* 157-216.

Chan J, Crowell E, Eder M*, et al.*, 2010. The rotation of cellulose synthase trajectories is microtubule dependent and influences the texture of epidermal cell walls in *Arabidopsis* hypocotyls. *J Cell Sci* **123**, 3490-5.

Cramer L, Mitchison T, 1995. Myosin is involved in postmitotic cell spreading. *J Cell Biol* **131**, 179-89.

Crowell EF, Bischoff V, Desprez T*, et al.*, 2009. Pausing of Golgi bodies on microtubules regulates secretion of cellulose synthase complexes in *Arabidopsis*. *Plant Cell* **21**, 1141-54.

Debolt S, Gutierrez R, Ehrhardt DW, Somerville C, 2007. Nonmotile cellulose synthase subunits repeatedly accumulate within localized regions at the plasma membrane in *Arabidopsis* hypocotyl cells following 2, 6-dichlorobenzonitrile treatment. *Plant Physiol* **145**, 334-8.

Desprez T, Juraniec M, Crowell EF*, et al.*, 2007. Organization of cellulose synthase complexes involved in primary cell wall synthesis in *Arabidopsis thaliana*. *Proc Natl Acad Sci USA* **104**, 15572-7.

Dubois M, Gilles KA, Hamilton JK, Rebers P, Smith F, 1956. Colorimetric method for determination of sugars and related substances. *Anal Chem* **28**, 350-6.

Fagard M, Desnos T, Desprez T*, et al.*, 2000. PROCUSTE1 encodes a cellulose synthase required for normal cell elongation specifically in roots and dark-grown hypocotyls of *Arabidopsis*. *Plant Cell* **12**, 2409-23.

Fedorov R, Böhl M, Tsiavaliaris G*, et al.*, 2009. The mechanism of pentabromopseudilin inhibition of myosin motor activity. *Nat Struct Mol Biol* **16**, 80-8.

Foth BJ, Goedecke MC, Soldati D, 2006. New insights into myosin evolution and classification. *Proc Natl Acad Sci USA* **103**, 3681-6.

Fujii S, Hayashi T, Mizuno K, 2010. Sucrose synthase is an integral component of the cellulose synthesis machinery. *Plant Cell Physiol* **51**, 294-301.

Fujita M, Himmelspach R, Ward J*, et al.*, 2013. The anisotropy1 D604N mutation in the *Arabidopsis* cellulose synthase1 catalytic domain reduces cell wall crystallinity and the velocity of cellulose synthase complexes. *Plant Physiol* **162**, 74-85.

Funaki K, Nagata A, Akimoto Y, Shimada K, Ito K, Yamamoto K, 2004. The motility of Chara corallina myosin was inhibited reversibly by 2, 3-butanedione monoxime (BDM). *Plant Cell Physiol* **45**, 1342-5.

Gibeaut DM, Carpita NC, 1991. Tracing cell wall biogenesis in intact cells and plants selective turnover and alteration of soluble and cell wall polysaccharides in grasses. *Plant Physiol* **97**, 551-61.

Green PB, 1962. Mechanism for plant cellular morphogenesis. *Science* **138**, 1404-5.

Gregory JD, 1955. The stability of N-ethylmaleimide and its reaction with sulfhydryl groups. *J Amer Chem Soc* **77**, 3922-3.

Gu Y, Kaplinsky N, Bringmann M*, et al.*, 2010. Identification of a cellulose synthase-associated protein required for cellulose biosynthesis. *Proc Natl Acad Sci USA* **107**, 12866-71.

Gutierrez R, Lindeboom JJ, Paredez AR, Emons AMC, Ehrhardt DW, 2009. *Arabidopsis* cortical microtubules position cellulose synthase delivery to the plasma membrane and interact with cellulose synthase trafficking compartments. *Nat Cell Biol* **11**, 797-806.

Harholt J, Suttangkakul A, Scheller HV, 2010. Biosynthesis of pectin. *Plant Physiol* **153**, 384-95.

Harpaz-Saad S, Mcfarlane HE, Xu S*, et al.*, 2011. Cellulose synthesis via the FEI2 RLK/SOS5 pathway and cellulose synthase 5 is required for the structure of seed coat mucilage in *Arabidopsis*. *Plant J* **68**, 941-53.

Henty JL, Bledsoe SW, Khurana P*, et al.*, 2011. *Arabidopsis* actin depolymerizing factor4 modulates the stochastic dynamic behavior of actin filaments in the cortical array of epidermal cells. *Plant Cell* **23**, 3711-26.

Herrmann C, Wray J, Travers F, Barman T, 1992. Effect of 2, 3-butanedione monoxime on myosin and myofibrillar ATPases. An example of an uncompetitive inhibitor. *Biochemistry* **31**, 12227-32.

Higaki T, Kutsuna N, Sano T, Kondo N, Hasezawa S, 2010. Quantification and cluster analysis of actin cytoskeletal structures in plant cells: role of actin bundling in stomatal movement during diurnal cycles in *Arabidopsis* guard cells. *Plant J* **61**, 156-65.

Hodge T, Jamie M, Cope T, 2000. A myosin family tree. *J Cell Sci* **113**, 3353-4.

Holland N, Holland D, Helentjaris T, Dhugga KS, Xoconostle-Cazares B, Delmer DP, 2000. A comparative analysis of the plant cellulose synthase (CesA) gene family. *Plant Physiol* **123**, 1313-24.

Islam K, Chin HF, Olivares AO, Saunders LP, De La Cruz EM, Kapoor TM, 2010. A myosin V inhibitor based on privileged chemical scaffolds. *Angew Chem* **122**, 8662-6.

Katz DB, Sussman MR, 1987. Inhibition and labeling of the plant plasma membrane H+-ATPase with N-ethylmaleimide. *Plant Physiol* **83**, 977-81.

Keegstra K, 2010. Plant cell walls. *Plant Physiol* **154**, 483-6.

Kimura S, Laosinchai W, Itoh T, Cui X, Linder CR, Brown RM, 1999. Immunogold labeling of rosette terminal cellulose-synthesizing complexes in the vascular plant Vigna angularis. *Plant Cell* **11**, 2075-85.

Konopka CA, Bednarek SY, 2008. Variable-angle epifluorescence microscopy: a new way to look at protein dynamics in the plant cell cortex. *Plant J* **53**, 186-96.

Ledbetter M, Porter K, 1963. A" microtubule" in plant cell fine structure. *J Cell Biol* **19**, 239-50.

Lei L, Li S, Du J, Bashline L, Gu Y, 2013. CELLULOSE SYNTHASE INTERACTIVE3 regulates cellulose biosynthesis in both a microtubule-dependent and microtubule-independent manner in *Arabidopsis*. *Plant Cell* **25**, 4912-23.

Lei L, Singh A, Bashline L, Li S, Yingling YG, Gu Y, 2015. CELLULOSE SYNTHASE INTERACTIVE1 Is Required for Fast Recycling of Cellulose Synthase Complexes to the Plasma Membrane in *Arabidopsis*. *Plant Cell* **27**, 2926-40.

Leucci MR, Di Sansebastiano G-P, Gigante M, Dalessandro G, Piro G, 2007. Secretion marker proteins and cell-wall polysaccharides move through different secretory pathways. *Planta* **225**, 1001-17.

Li J, Arieti R, Staiger CJ, 2014. Actin filament dynamics and their role in plant cell expansion. In. *Plant Cell Wall Patterning and Cell Shape.* 127-62.

Li JF, Nebenführ A, 2008. The tail that wags the dog: the globular tail domain defines the function of myosin V/XI. *Traffic* **9**, 290-8.

Li S, Lei L, Somerville CR, Gu Y, 2012. Cellulose synthase interactive protein 1 (CSI1) links microtubules and cellulose synthase complexes. *Proc Natl Acad Sci USA* **109**, 185-90.

Li S, Lei L, Yingling YG, Gu Y, 2015. Microtubules and cellulose biosynthesis: the emergence of new players. *Curr Opin Plant Biol* **28**, 76-82.

Li T, Sperelakis N, Teneick RE, Solaro R, 1985. Effects of diacetyl monoxime on cardiac excitation-contraction coupling. *J Pharmacol Exp Ther* **232**, 688-95.

Liebe S, Menzel D, 1995. Actomyosin-based motility of endoplasmic reticulum and chloroplasts in *Vallisneria* mesophyll cells. *Biol Cell* **85**, 207-22.

Luo Y, Scholl S, Doering A*, et al.*, 2015. V-ATPase activity in the TGN/EE is required for exocytosis and recycling in *Arabidopsis*. *Nat Plant* **1**.

Lymn R, Taylor E, 1971. Mechanism of adenosine triphosphate hydrolysis by actomyosin. *Biochemistry* **10**, 4617-24.

Madison SL, Buchanan ML, Glass JD, Mcclain TF, Park E, Nebenführ A, 2015. Class XI myosins move specific organelles in pollen tubes and are required for normal fertility and pollen tube growth in *Arabidopsis*. *Plant Physiol* **169**, 1946-60.

Mccurdy D, Harmon A, 1992. Phosphorylation of a putative myosin light chain in *Chara* by calcium-dependent protein kinase. *Protoplasma* **171**, 85-8.

Mccurdy DW, 1999. Is 2, 3-butanedione monoxime an effective inhibitor of myosin-based activities in plant cells? *Protoplasma* **209**, 120-5.

Mcfarlane HE, Döring A, Persson S, 2014. The cell biology of cellulose synthesis. *Annu Rev Plant Biol* **65**, 69-94.

Mckillop D, Fortune N, Ranatunga K, Geeves M, 1994. The influence of 2, 3-butanedione 2-monoxime (BDM) on the interaction between actin and myosin in solution and in skinned muscle fibres. *J Muscle Res Cell Motil* **15**, 309-18.

Mei Y, Gao H-B, Yuan M, Xue H-W, 2012. The *Arabidopsis* ARCP protein, CSI1, which is required for microtubule stability, is necessary for root and anther development. *Plant Cell* **24**, 1066-80.

Molchan TM, Valster AH, Hepler PK, 2002. Actomyosin promotes cell plate alignment and late lateral expansion in *Tradescantia* stamen hair cells. *Planta* **214**, 683-93.

Morgan JL, Strumillo J, Zimmer J, 2013. Crystallographic snapshot of cellulose synthesis and membrane translocation. *Nature* **493**, 181-6.

Morimatsu M, Hasegawa S, Higashi-Fujime S, 2002. Protein phosphorylation regulates actomyosin-driven vesicle movement in cell extracts isolated from the green algae, *Chara corallina*. *Cell Motil Cytoskeleton* **53**, 66-76.

Morré DJ, Brightman AO, Hidalgo A, Navas P, 1995. Selective inhibition of auxin-stimulated NADH oxidase activity and elongation growth of soybean hypocotyls by thiol reagents. *Plant Physiol* **107**, 1285-91.

Mueller SC, Brown Jr RM, Scott TK, 1976. Cellulosic microfibrils: nascent stages of synthesis in a higher plant cell. *Science* **194**, 949-51.

Mueller SC, Brown RM, 1980. Evidence for an intramembrane component associated with a cellulose microfibril-synthesizing complex in higher plants. *J Cell Biol* **84**, 315-26.

Mühlhausen S, Kollmar M, 2013. Whole genome duplication events in plant evolution reconstructed and predicted using myosin motor proteins. *BMC Evol Biol* **13**, 202.

Nagawa S, Xu T, Lin D*, et al.*, 2012. ROP GTPase-dependent actin microfilaments promote PIN1 polarization by localized inhibition of clathrin-dependent endocytosis. *PLoS Biol* **10**, e1001299.

Nebenführ A, Gallagher LA, Dunahay TG*, et al.*, 1999. Stop-and-go movements of plant Golgi stacks are mediated by the acto-myosin system. *Plant Physiol* **121**, 1127-41.

Ojangu E-L, Tanner K, Pata P*, et al.*, 2012. Myosins XI-K, XI-1, and XI-2 are required for development of pavement cells, trichomes, and stigmatic papillae in *Arabidopsis*. *BMC Plant Biol* **12**, 81.

Paredez AR, Persson S, Ehrhardt DW, Somerville CR, 2008. Genetic evidence that cellulose synthase activity influences microtubule cortical array organization. *Plant Physiol* **147**, 1723-34.

Paredez AR, Somerville CR, Ehrhardt DW, 2006. Visualization of cellulose synthase demonstrates functional association with microtubules. *Science* **312**, 1491-5.

Park E, Nebenführ A, 2013. Myosin XIK of *Arabidopsis thaliana* accumulates at the root hair tip and is required for fast root hair growth. *PloS one* **8**, e76745.

Paves H, Truve E, 2007. Myosin inhibitors block accumulation movement of chloroplasts in *Arabidopsis* thaliana leaf cells. *Protoplasma* **230**, 165-9.

Pear JR, Kawagoe Y, Schreckengost WE, Delmer DP, Stalker DM, 1996. Higher plants contain homologs of the bacterial celA genes encoding the catalytic subunit of cellulose synthase. *Proc Natl Acad Sci USA* **93**, 12637-42.

Peremyslov VV, Cole RA, Fowler JE, Dolja VV, 2015. Myosin-powered membrane compartment drives cytoplasmic streaming, cell expansion and plant development. *PloS one* **10**, e0139331.

Peremyslov VV, Klocko AL, Fowler JE, Dolja VV, 2012. *Arabidopsis* myosin XI-K localizes to the motile endomembrane vesicles associated with F-actin. *Front Plant Sci* **3**.

Peremyslov VV, Morgun EA, Kurth EG, Makarova KS, Koonin EV, Dolja VV, 2013. Identification of myosin XI receptors in *Arabidopsis* defines a distinct class of transport vesicles. *Plant Cell* **25**, 3022-38.

Peremyslov VV, Prokhnevsky AI, Avisar D, Dolja VV, 2008. Two class XI myosins function in organelle trafficking and root hair development in *Arabidopsis*. *Plant Physiol* **146**, 1109-16.

Peremyslov VV, Prokhnevsky AI, Dolja VV, 2010. Class XI myosins are required for development, cell expansion, and F-Actin organization in *Arabidopsis*. *Plant Cell* **22**, 1883-97.

Persson S, Paredez A, Carroll A*, et al.*, 2007. Genetic evidence for three unique components in primary cell-wall cellulose synthase complexes in *Arabidopsis*. *Proc Natl Acad Sci USA* **104**, 15566-71.

Preller M, Chinthalapudi K, Martin R, KnöLker H-J, Manstein DJ, 2011. Inhibition of myosin ATPase activity by halogenated pseudilins: a structure–activity study. *J Med Chem* **54**, 3675-85.

Prokhnevsky AI, Peremyslov VV, Dolja VV, 2008. Overlapping functions of the four class XI myosins in *Arabidopsis* growth, root hair elongation, and organelle motility. *Proc Natl Acad Sci USA* **105**, 19744-9.

Richards TA, Cavalier-Smith T, 2005. Myosin domain evolution and the primary divergence of eukaryotes. *Nature* **436**, 1113-8.

Richmond T, 2000. Higher plant cellulose synthases. *Genome Biol* **1**, 3001.1-.6.

Roudier F, Fernandez AG, Fujita M*, et al.*, 2005. COBRA, an *Arabidopsis* extracellular glycosyl-phosphatidyl inositol-anchored protein, specifically controls highly anisotropic expansion through its involvement in cellulose microfibril orientation. *Plant Cell* **17**, 1749-63.

Saitoh M, Ishikawa T, Matsushima S, Naka M, Hidaka H, 1987. Selective inhibition of catalytic activity of smooth muscle myosin light chain kinase. *J Biol Chem* **262**, 7796-801.

Sampathkumar A, Gutierrez R, Mcfarlane HE*, et al.*, 2013. Patterning and lifetime of plasma membrane-localized cellulose synthase is dependent on actin organization in *Arabidopsis* interphase cells. *Plant Physiol* **162**, 675-88.

Sampathkumar A, Lindeboom JJ, Debolt S*, et al.*, 2011. Live cell imaging reveals structural associations between the actin and microtubule cytoskeleton in *Arabidopsis*. *Plant Cell* **23**, 2302-13.

Sampathkumar A, Wightman R, 2015. Live cell imaging of the cytoskeleton and cell wall enzymes in plant cells. In. *Plant Cell Expansion.* Springer, 133-41.

Scheller HV, Ulvskov P, 2010. Hemicelluloses. *Annu Rev Plant Biol* **61**, 263.

Schindelman G, Morikami A, Jung J*, et al.*, 2001. COBRA encodes a putative GPI-anchored protein, which is polarly localized and necessary for oriented cell expansion in *Arabidopsis*. *Gene Dev* **15**, 1115-27.

Sekine T, Barnett L, Kielley WW, 1962. The active site of myosin adenosine triphosphatase I. Localization of one of the sulfhydryl groups. *J Biol Chem* **237**, 2769-72.

Shaw SL, Kamyar R, Ehrhardt DW, 2003. Sustained microtubule treadmilling in *Arabidopsis* cortical arrays. *Science* **300**, 1715-8.

Sheahan MB, Staiger CJ, Rose RJ, Mccurdy DW, 2004. A green fluorescent protein fusion to actin-binding domain 2 of *Arabidopsis* fimbrin highlights new features of a dynamic actin cytoskeleton in live plant cells. *Plant Physiol* **136**, 3968-78.

Somerville C, 2006. Cellulose synthesis in higher plants. *Annu Rev Cell Dev Biol* **22**, 53-78.

Sparkes IA, Teanby NA, Hawes C, 2008. Truncated myosin XI tail fusions inhibit peroxisome, Golgi, and mitochondrial movement in tobacco leaf epidermal cells: a genetic tool for the next generation. *J Exp Bot* **59**, 2499-512.

Staiger CJ, Sheahan MB, Khurana P, Wang X, Mccurdy DW, Blanchoin L, 2009. Actin filament dynamics are dominated by rapid growth and severing activity in the *Arabidopsis* cortical array. *J Cell Biol* **184**, 269-80.

Stapleton MT, Fuchsbauer CM, Allshire AP, 1998. BDM drives protein dephosphorylation and inhibits adenine nucleotide exchange in cardiomyocytes. *Am J Physiol Heart Circ Physiol* **275**, H1260-H6.

Syamaladevi DP, Spudich JA, Sowdhamini R, 2012. Structural and functional insights on the Myosin superfamily. *Bioinform Biol Insights* **6**, 11.

Taylor NG, Howells RM, Huttly AK, Vickers K, Turner SR, 2003. Interactions among three distinct CesA proteins essential for cellulose synthesis. *Proc Natl Acad Sci USA* **100**, 1450-5.

Tominaga M, Kimura A, Yokota E*, et al.*, 2013. Cytoplasmic streaming velocity as a plant size determinant. *Dev Cell* **27**, 345-52.

Tominaga M, Yokota E, Sonobe S, Shimmen T, 2000. Mechanism of inhibition of cytoplasmic streaming by a myosin inhibitor, 2, 3-butanedione monoxime. *Protoplasma* **213**, 46-54.

Ueda H, Yokota E, Kutsuna N*, et al.*, 2010. Myosin-dependent endoplasmic reticulum motility and F-actin organization in plant cells. *Proc Natl Acad Sci USA* **107**, 6894-9.

Updegraff DM, 1969. Semimicro determination of cellulose inbiological materials. *Anal Biochem* **32**, 420-4.

Vain T, Crowell EF, Timpano H*, et al.*, 2014. The cellulase KORRIGAN is part of the cellulose synthase complex. *Plant Physiol* **165**, 1521-32.

Vale RD, Milligan RA, 2000. The way things move: looking under the hood of molecular motor proteins. *Science* **288**, 88-95.

Wallace IS, Somerville CR, 2014. A blueprint for cellulose biosynthesis, deposition, and regulation in plants. In. *Plant Cell Wall Patterning and Cell Shape.* 65-95.

Watanabe Y, Meents M, Mcdonnell L*, et al.*, 2015. Visualization of cellulose synthases in *Arabidopsis* secondary cell walls. *Science* **350**, 198-203.

Wightman R, Marshall R, Turner SR, 2009. A cellulose synthase-containing compartment moves rapidly beneath sites of secondary wall synthesis. *Plant Cell Physiol* **50**, 584-94.

Wightman R, Turner SR, 2008. The roles of the cytoskeleton during cellulose deposition at the secondary cell wall. *Plant J* **54**, 794-805.

Yamamoto K, Hamada S, Kashiyama T, 1999. Myosins from plants. *Cell Mol Life Sci* **56**, 227-32.

Yang L, Qin L, Liu G, Peremyslov VV, Dolja VV, Wei Y, 2014. Myosins XI modulate host cellular responses and penetration resistance to fungal pathogens. *Proc Natl Acad Sci USA* **111**, 13996-4001.

Yokota E, Muto S, Shimmen T, 1999a. Inhibitory regulation of higher-plant myosin by Ca^{2+} ions. *Plant Physiol* **119**, 231-40.

Yokota E, Yukawa C, Muto S, Sonobe S, Shimmen T, 1999b. Biochemical and immunocytochemical characterization of two types of myosins in cultured tobacco bright yellow-2 cells. *Plant Physiol* **121**, 525-34.

PUBLICATION

PUBLICATION

Cai, C., Henty-Ridilla, J. L., Szymanski, D. B., & Staiger, C. J. (2014). *Arabidopsis* myosin XI: a motor rules the tracks. *Plant Physiol*, *166*(3), 1359-1370.**

(http://www.plantphysiol.org/, Copyright American Society of Plant Biologists)

** Experiements were designed by C.J.S, C.C., D.B.S, and J.L.H-R. Work was performed by C.C. and J.L.H-R. (developing quantitative tool for actin architecture analysis, and perform the initial actin organization measurement in the *xi3KO* mutant). The manuscript was written by C.C. and C.J.S. with great input from D.B.S. This work was supported by the Center for Direct Catalytic Conversion of Biomass to Biofuels, an Energy Frontier Research Center funded by the U.S. Department of Energy, Office of Science, Basic Energy Sciences (award no. DE–SC0000997). The TIRF microscopy facility at Purdue was funded in part by the Bindley Bioscience Center.

Arabidopsis Myosin XI: A Motor Rules the Tracks[1][C][W][OPEN]

Chao Cai, Jessica L. Henty-Ridilla, Daniel B. Szymanski, and Christopher J. Staiger*

Department of Biological Sciences (C.C., J.L.H.-R., C.J.S.), Center for the Direct Catalytic Conversion of Biomass to Biofuels (C.C., J.L.H.-R., D.B.S., C.J.S.), and Department of Agronomy (D.B.S.), Purdue University, West Lafayette, Indiana 47907

Plant cell expansion relies on intracellular trafficking of vesicles and macromolecules, which requires myosin motors and a dynamic actin network. Arabidopsis (*Arabidopsis thaliana*) myosin XI powers the motility of diverse cellular organelles, including endoplasmic reticulum, Golgi, endomembrane vesicles, peroxisomes, and mitochondria. Several recent studies show that there are changes in actin organization and dynamics in *myosin xi* mutants, indicating that motors influence the molecular tracks they use for transport. However, the mechanism by which actin organization and dynamics are regulated by myosin XI awaits further detailed investigation. Here, using high spatiotemporal imaging of living cells, we quantitatively assessed the architecture and dynamic behavior of cortical actin arrays in a mutant with three *Myosin XI* (*XI-1*, *XI-2*, and *XI-K*) genes knocked out (*xi3KO*). In addition to apparent reduction of organ and cell size, the mutant showed less dense and more bundled actin filament arrays in epidermal cells. Furthermore, the overall actin dynamicity was significantly inhibited in the *xi3KO* mutant. Because cytoskeletal remodeling is contributed mainly by filament assembly/disassembly and translocation/buckling, we also examined the dynamic behavior of individual actin filaments. We found that the *xi3KO* mutant had significantly decreased actin turnover, with a 2-fold reduction in filament severing frequency. Moreover, quantitative analysis of filament shape change over time revealed that myosin XI generates the force for buckling and straightening of both single actin filaments and actin bundles. Thus, our data provide genetic evidence that three Arabidopsis class XI myosins contribute to actin remodeling by stimulating turnover and generating the force for filament shape change.

Active transport is an important mechanism for eukaryotic cells to maintain the proper distribution of organelles and macromolecules and to deliver materials to sites of polar growth. Unlike animal cells, which use microtubules as tracks for long-distance transport, plants use predominantly actin filaments and myosin motors for vesicle trafficking and organelle positioning (Schuh, 2011). Studies using dominant-negative, RNAi, and knockout mutants indicate that the plant class XI myosins are motor molecules involved in transport of organelles, such as endoplasmic reticulum, Golgi, mitochondria, and peroxisomes (Avisar et al., 2008, 2009; Peremyslov et al., 2008, 2010; Prokhnevsky et al., 2008; Sparkes et al., 2008).

In addition to myosin XI, a functional network of dynamic actin filaments is critical for vesicle trafficking. Actin filaments or bundles provide the tracks for myosins to processively translocate using the energy of ATP hydrolysis. In Arabidopsis (*Arabidopsis thaliana*) epidermal cells, cortical actin filament arrays undergo continuous and rapid remodeling (Staiger et al., 2009; Smertenko et al., 2010). Two main features contribute to this dynamic rearrangement of actin filaments: translocation and buckling, and rapid assembly and disassembly (Staiger et al., 2009; Henty-Ridilla et al., 2013). The organization and dynamic behavior of actin filaments are regulated by a plethora of actin-binding proteins (Henty-Ridilla et al., 2013). Myosin is both a motor that drives long-distance cargo motility and also an actin regulator. In vitro biochemical assays show that skeletal muscle myosin II can induce the disassembly and fragmentation of actin filaments (Murrell and Gardel, 2012; Vogel et al., 2013). In budding yeast (*Saccharomyces cerevisiae*), myosin V is involved in the rapid translocation of actin cables and is responsible for the delivery of formin regulators, which affects the assembly of actin filaments at specific subcellular locations (Chesarone-Cataldo et al., 2011; Yu et al., 2011). By contrast, our understanding of how plant myosins are involved in the regulation of actin filament turnover and translocation is incomplete.

Studies on the effects of myosin on actin organization and dynamics in plant cells were initially performed by applying the drug 2,3-butanedione monoxime (BDM), which inhibits ATP hydrolysis by the myosin II head domain (Herrmann et al., 1992). For example, treatment with BDM alters actin organization in tip-growing root

[1] This work was supported by the Center for Direct Catalytic Conversion of Biomass to Biofuels, an Energy Frontier Research Center funded by the U.S. Department of Energy, Office of Science, Basic Energy Sciences (award no. DE–SC0000997).

* Address correspondence to staiger@purdue.edu.

The author responsible for distribution of materials integral to the findings presented in this article in accordance with the policy described in the Instructions for Authors (www.plantphysiol.org) is: Christopher J. Staiger (staiger@purdue.edu).

[C] Some figures in this article are displayed in color online but in black and white in the print edition.

[W] The online version of this article contains Web-only data.

[OPEN] Articles can be viewed online without a subscription.

www.plantphysiol.org/cgi/doi/10.1104/pp.114.244335

hairs and pollen tubes (Tominaga et al., 2000; Zheng et al., 2009), as well as in cells of the root transition zone (Šamaj et al., 2000). A detailed description of the dynamic behavior of individual actin filaments in epidermal cells shows that BDM inhibits the turnover and shape change of actin filaments (Staiger et al., 2009). Although there is evidence that BDM can inhibit the motility of plant myosin XI in vitro (Tominaga et al., 2000; Funaki et al., 2004), this drug is typically applied at millimolar concentrations and probably does not inhibit all myosin-dependent cellular processes in plant cells (McCurdy, 1999). Therefore, genetic approaches using knockout mutants are important to interrogate the function of plant myosins. In Arabidopsis, actin filament bundles are oriented more transversely in *myosin xi* double, triple, and quadruple mutants compared with the predominantly longitudinal orientation in wild-type cells (Peremyslov et al., 2010; Ueda et al., 2010). Moreover, overall actin dynamics are reduced in root hairs of a *myosin xi-k* mutant (Park and Nebenführ, 2013). Also, actin filament arrays appear more randomized in tip-growing *Physcomitrella patens* protonemal cells when both *myosin xi* genes are knocked down (Vidali et al., 2010). Surprisingly, the overall dynamicity of the actin network is not altered in *Myosin XI* knockdown protonemal cells (Vidali et al., 2010). To gain a better understanding of the mechanism by which myosins impact actin filament organization and dynamics in plant cells, detailed analyses of actin filament properties in *myosin* mutants are necessary.

Here, we used a previously characterized *myosin xi-1*, *xi-2*, and *xi-k* triple knockout mutant (Peremyslov et al., 2010), combined with advanced live-cell imaging, to dissect how Arabidopsis myosin XI is involved in actin remodeling. With the high temporal and spatial resolution afforded by variable-angle epifluorescence microscopy (VAEM) and a set of metrics for analyzing filament dynamics, we found that the three class XI myosins generate force for the buckling and straightening of actin filaments and bundles, as well as promote actin filament turnover.

RESULTS

The Growth of Arabidopsis Seedlings Is Inhibited in a *myosin xi* Triple Knockout Mutant

Recently, it was reported that the velocity of myosin-dependent motility correlates with plant size, and knockout mutants of Arabidopsis *myosins* exhibit reduced organ size (Peremyslov et al., 2010; Tominaga et al., 2013). We analyzed the function of myosin XI in Arabidopsis seedlings using a previously characterized triple mutant line with *myosin xi-1*, *myosin xi-2*, and *myosin xi-k* knocked out (*xi3KO*; Peremyslov et al., 2010). To confirm that the loss of multiple myosin XI isoforms affected the expansion of organs, etiolated hypocotyls of the *xi3KO* mutant were examined. Organ length was significantly reduced in hypocotyls of *xi3KO* mutant seedlings compared with the wild type over a developmental time series (Fig. 1, A and B). We also examined light-grown roots. The length of roots from *xi3KO* seedlings was significantly reduced compared with the wild type (Fig. 1, C and D), which is consistent with a previous study (Peremyslov et al., 2010).

To test whether the reduction of organ length in the *xi3KO* mutant is due to inhibition of cell expansion, the length of epidermal cells from hypocotyls and the root elongation zone was measured. The growth of Arabidopsis hypocotyl epidermal cells occurs along a gradient, with cells at the base (near the root) finishing axial expansion earlier than those near the apex (near the cotyledons; Gendreau et al., 1997). The length and width of epidermal cells from both apical and basal regions of 5-d-old hypocotyls were significantly reduced in the *xi3KO* mutant (Fig. 1, E and F). Similarly, epidermal cells from the root elongation zone exhibited reduced length and width in the *xi3KO* mutant compared with the wild type (Fig. 1, G and H). These results suggest that loss of myosin XI inhibited cell and organ expansion in the early developmental stage.

The Architecture of Cortical Actin Arrays Is Altered in Epidermal Cells of the *xi3KO* Mutant

Myosins may have the ability to generate force on a preexisting actin network (Szymanski and Cosgrove, 2009) and Arabidopsis class XI myosins are reportedly involved in regulating actin organization (Peremyslov et al., 2010; Ueda et al., 2010). In *myosin xi* double, triple, and quadruple mutants, actin bundles appear to be more transversely oriented compared with the longitudinal orientation in wild-type cells (Peremyslov et al., 2010; Ueda et al., 2010). To further test whether the loss of myosin XI affects actin organization, we examined the cortical actin arrays in Arabidopsis seedlings expressing the yellow fluorescent protein fused with the second actin-binding domain from Arabidopsis FIMBRIN1 (YFP-fABD2) with VAEM. Representative images of epidermal cells from *xi3KO* hypocotyls showed that the cortical actin array was much less dense and more bundled compared with wild-type cells (Fig. 2A). Quantitative analyses were performed to analyze the architecture of cortical actin arrays. Two parameters, skewness and density, were measured to evaluate the extent of bundling and the percentage of occupancy of actin filaments in epidermal cells (Higaki et al., 2010; Henty et al., 2011; Li et al., 2012). The *xi3KO* mutant had a significantly reduced percentage of occupancy and increased bundling of actin arrays in both the apical and basal regions of the hypocotyl (Fig. 2, B and C). We also examined the angle of actin filaments with respect to the longitudinal axis of the cell, as well as the parallelness of actin filaments with respect to each other, using the methods of Ueda et al. (2010). The *xi3KO* mutant had a significantly increased angle in both apical and basal regions

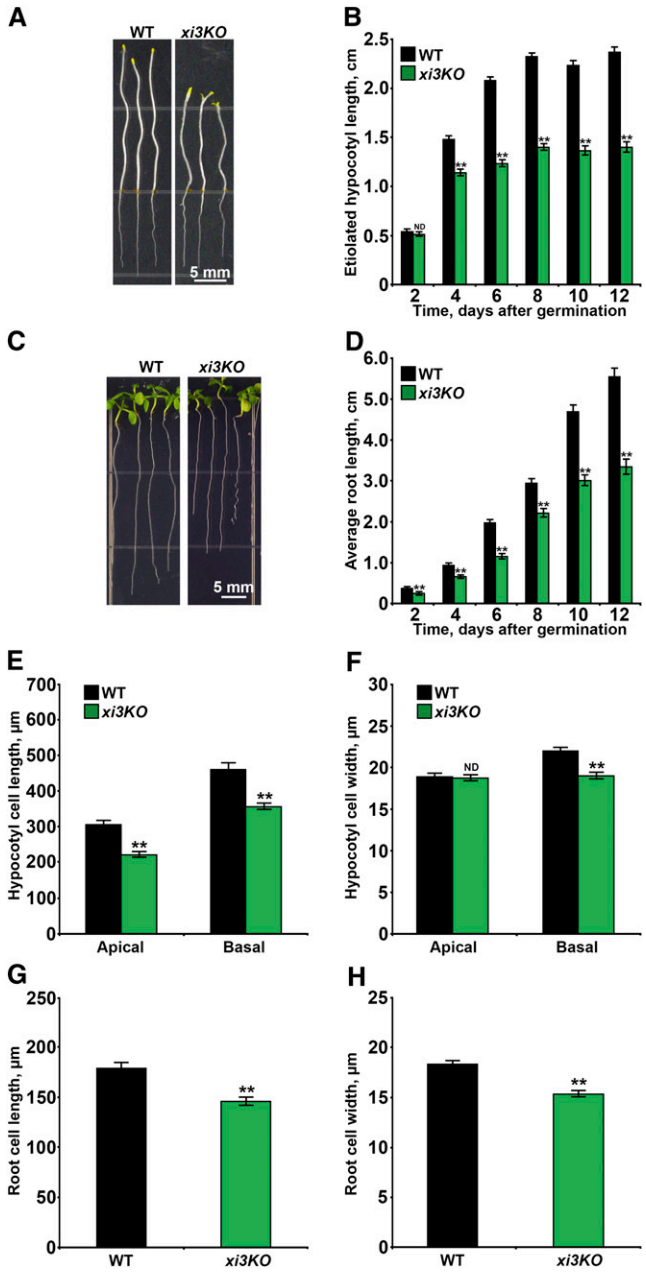

Figure 1. The myosin *xi3KO* mutant has reduced hypocotyl, root, and epidermal cell length. A, Representative examples of etiolated Arabidopsis seedlings from 5-d-old *myosin xi-1, xi-2, xi-k* triple knockout (*xi3KO*) mutant and the wild type (WT) are shown. Bar = 5 mm. B, The length of etiolated hypocotyls was significantly reduced in the *xi3KO* mutant compared with the wild type. Measurements were taken on alternate days for 12 d total. Values are means ± SE ($n \geq 50$ hypocotyls per genotype; Student's *t* test, $^{**}P < 0.01$). C, Representative examples of light-grown seedlings from 7-d-old *xi3KO* mutant and the wild type are shown. Bar = 5 mm. D, The length of light-grown roots was significantly reduced in the *xi3KO* mutant compared with the wild type. Measurements were performed on alternate days. Values are means ± SE ($n \geq 50$ roots per genotype; Student's *t* test, $^{**}P < 0.01$). E, The length of epidermal cells was measured at the apex (near cotyledons) and base (near root) of 5-d-old etiolated hypocotyls. The *xi3KO* mutant had significantly reduced epidermal cell length at both apex and base of the hypocotyl (Fig. 2D) and significantly reduced filament-filament parallelness in the basal region of the hypocotyl (Fig. 2E), suggesting that actin filament arrays in the *xi3KO* mutant are more transversely oriented and disorganized.

To examine whether the change in architecture of actin arrays is apparent in other organs, the extent of bundling and the percentage of occupancy of actin filaments were also evaluated in light-grown roots of the *xi3KO* mutant. The actin arrays were more bundled and less dense in epidermal cells from the root elongation zone (Fig. 3, A–C), which is consistent with the result in hypocotyls. We also examined overall filament orientation and filament parallelness in root epidermal cells. The actin filament arrays showed an increase of both angle and parallelness in epidermal cells from the root elongation zone (Fig. 3, D and E). Collectively, these results demonstrate that the three class XI myosins are involved in regulation of actin organization.

Cortical Actin Array Dynamics in Epidermal Cells Are Reduced in the *xi3KO* Mutant

Cortical actin arrays in Arabidopsis hypocotyl epidermal cells undergo constant remodeling and filament turnover (Staiger et al., 2009; Smertenko et al., 2010). It has been reported that knocking down *Myosin XI* in *Physcomitrella patens* protonemal cells does not affect the overall dynamics of actin organization (Vidali et al., 2010). To analyze whether the overall dynamicity of cortical actin arrays is altered in Arabidopsis when three *Myosin XI* genes are knocked out, time-lapse VAEM series were collected from epidermal cells of etiolated hypocotyls expressing YFP-fABD2. Actin arrays in the epidermal cells from the *xi3KO* mutant appeared to be much less dynamic when compared with wild-type cells at both apical and basal regions of the hypocotyl (Fig. 4A). To quantify global actin dynamics, a correlation coefficient analysis was performed (Vidali et al., 2010). This analysis was accomplished by calculating pixel intensity correlation for all pairwise temporal intervals from multiple time-lapse series. The overall

of the hypocotyl. Values are means ± SE ($n > 70$ cells from at least 10 hypocotyls per genotype; Student's *t* test, $^{**}P < 0.01$). F, The width of epidermal cells was measured at the apex and base of the same hypocotyls in E. The *xi3KO* mutant had significantly reduced epidermal cell width at the basal region of the hypocotyl. Values are means ± SE ($n > 100$ cells from at least 10 hypocotyls per genotype; Student's *t* test, $^{**}P < 0.01$). G, The length of epidermal cells was measured from the elongation zone of 10-d-old light-grown roots. The *xi3KO* mutant had significantly reduced epidermal cell length. Values are means ± SE ($n > 80$ cells from at least 10 roots per genotype; Student's *t* test, $^{**}P < 0.01$). H, The width of epidermal cells was measured at the elongation zone of the same roots in G. The *xi3KO* mutant had significantly reduced epidermal cell width. Values are means ± SE ($n > 100$ cells from at least 10 roots per genotype Student's *t* test, $^{**}P < 0.01$). ND, No significant difference.

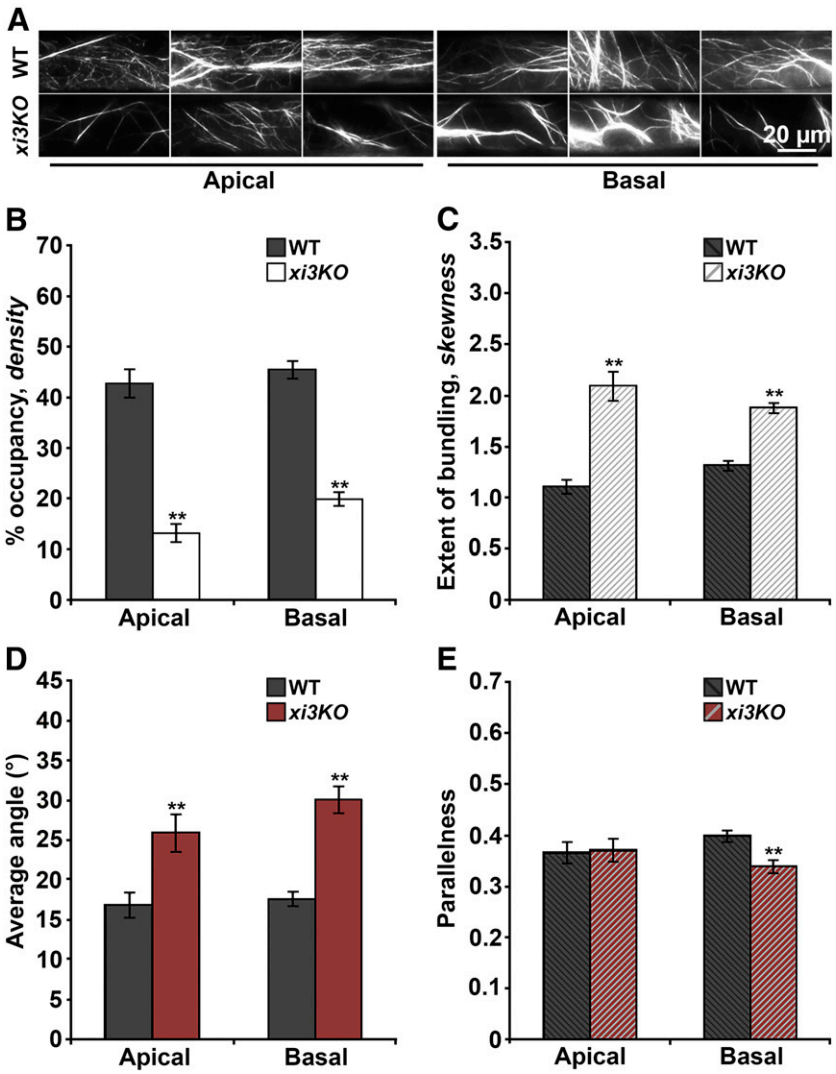

Figure 2. The architecture of actin arrays in epidermal cells of the *xi3KO* mutant is altered. A, Representative images of epidermal cells from 5-d-old dark-grown hypocotyls of wild-type (WT) and *xi3KO* seedlings expressing YFP-fABD2. VAEM images were collected from the apical and basal regions of the hypocotyl. Bar = 20 μm. B and C, Quantitative analyses of the architecture of cortical actin arrays in wild-type and *xi3KO* mutant epidermal cells. B, Percentage of occupancy (density) was measured. Filament density was significantly decreased in epidermal cells at both apical and basal regions of hypocotyls in the *xi3KO* mutant compared with the wild type. Values given are means ± SE ($n \geq 150$ images from 30 hypocotyls per genotype; Student's *t* test, $^{**}P < 0.01$). C, The extent of filament bundling (skewness) was measured. Bundling was significantly increased in epidermal cells at both apical and basal regions of the hypocotyl in *xi3KO*. The same images used for B were analyzed for bundling (Student's *t* test, $^{**}P < 0.01$). D and E, Quantitative analyses of the orientation of cortical actin arrays in wild-type and *xi3KO* mutant epidermal cells. D, Average angle of actin filaments with respect to the longitudinal axis of epidermal cells was measured. Angle was significantly increased in epidermal cells at both apical and basal regions of hypocotyls in the *xi3KO* mutant compared with the wild type. Values given are means ± SE (Student's *t* test, $^{**}P < 0.01$). E, The parallelness of actin filaments with respect to each other was measured. Parallelness was significantly reduced in epidermal cells at the basal regions of the hypocotyl in *xi3KO* compared with the wild type. The same images used for B and C were analyzed for angle and parallelness (Student's *t* test, $^{**}P < 0.01$).

actin dynamics is reflected by the rate of decay of correlation coefficient values as a function of time interval. A faster decay of the curve suggests more active actin dynamics. The correlation coefficient curve for the *xi3KO* mutant decayed significantly slower compared with the wild type (Fig. 4, B and C), indicating decreased dynamics of the actin arrays in *xi3KO* mutant cells. Both apical and basal regions of the dark-grown hypocotyl showed a reduction in actin dynamicity, indicating that myosin XI regulates actin dynamics at different developmental stages. Moreover, we measured the overall dynamicity for different subpopulations of actin filaments. The correlation coefficient curves for both single actin filaments and actin bundles decayed significantly slower in the *xi3KO* mutant compared with the wild type (Supplemental Fig. S1, C–F; Supplemental Methods S1), indicating that these three myosins XI are involved in regulating the dynamics of both single actin filament and actin bundles. We also applied BDM, a myosin ATPase inhibitor, on hypocotyl epidermal cells expressing GFP-fABD2. The correlation coefficient curves decayed significantly slower and in a dose-dependent manner after 5-min treatments with different concentrations of BDM (Fig. 4, D and E), thus phenocopying the *xi3KO* mutant.

To test whether the reduction of overall dynamics in *xi3KO* occurs in other organs and developmental states, we examined the correlation coefficient of time-lapse images collected from epidermal cells in the elongation zone of light-grown roots. The results show that the overall dynamicity of actin arrays in *xi3KO* root epidermal cells was reduced compared with the wild type (Fig. 3F), which is consistent with the result from hypocotyls. Collectively, these data indicate that three Arabidopsis myosin XI isoforms are involved in promoting the overall dynamicity of actin filament arrays.

The Dynamic Properties of Single Actin Filaments Are Altered in the *xi3KO* Mutant

Two main features contribute to the dynamic behavior of actin filaments in the cortical array of epidermal

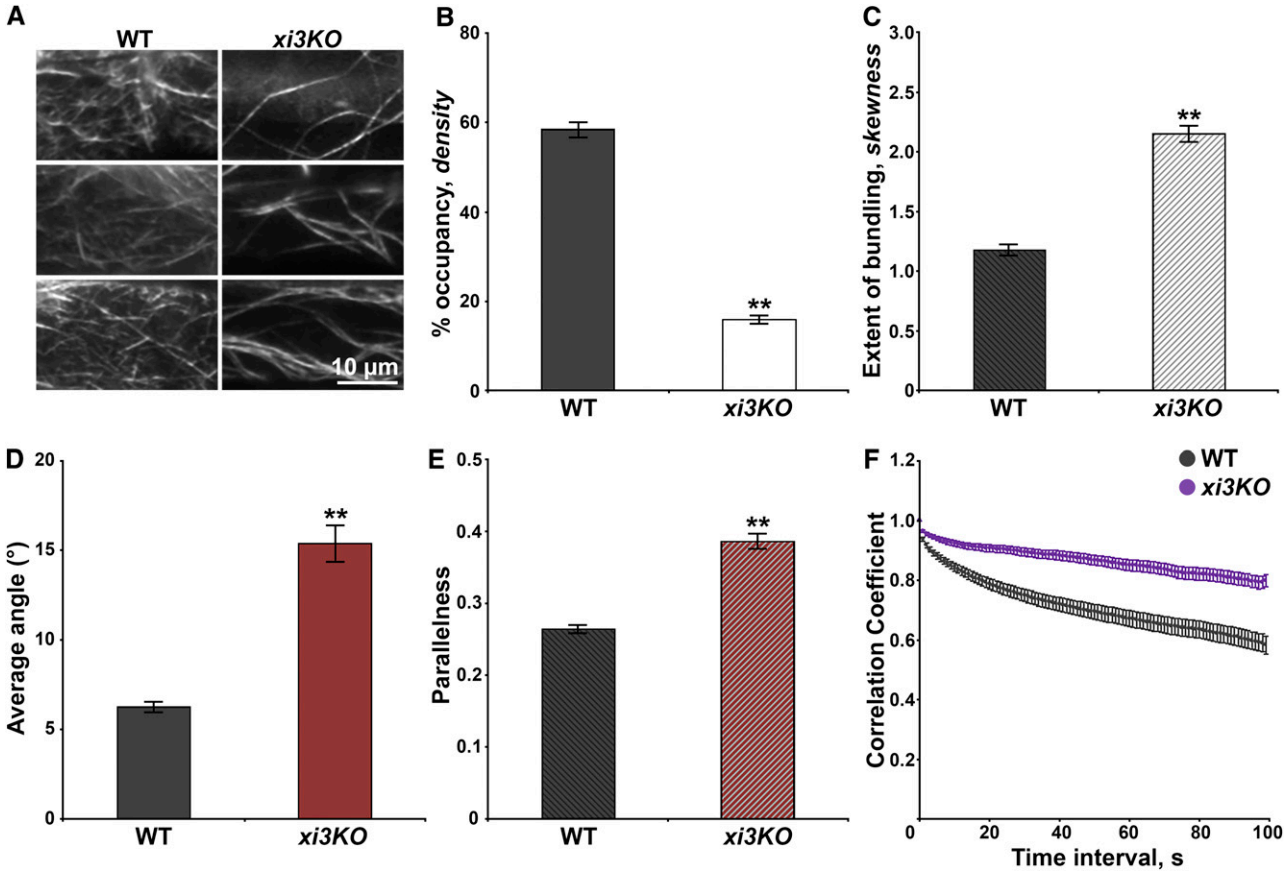

Figure 3. The architecture and overall dynamicity of actin arrays in epidermal cells from the root elongation zone of the *xi3KO* mutant are changed. A, Representative images of epidermal cells from 7-d-old light-grown roots of wild-type (WT) and *xi3KO* seedlings expressing YFP-fABD2. VAEM images were collected from the elongation zone of the root. Bar = 10 μm. B and C, Quantitative analyses of the architecture of actin arrays in wild-type and *xi3KO* mutant epidermal cells. B, Percentage of occupancy (density) was measured. Filament density was significantly decreased in the *xi3KO* mutant compared with the wild type. Values given are means ± SE ($n \geq 100$ images from 30 seedlings per genotype; Student's *t* test, $^{**}P < 0.01$). C, The extent of filament bundling (skewness) was measured. Bundling was significantly increased in the *xi3KO* mutant compared with the wild type. The same images used for B were analyzed for bundling (Student's *t* test, $^{**}P < 0.01$). D and E, Quantitative analyses of the orientation of cortical actin arrays in wild-type and *xi3KO* mutant epidermal cells. D, Average angle of actin filaments with respect to the longitudinal axis of epidermal cells was measured. Angle was significantly increased in the *xi3KO* mutant compared with the wild type. Values given are means ± SE (Student's *t* test, $^{**}P < 0.01$). E, The parallelness of actin filaments with respect to each other was measured. Parallelness was significantly increased in *xi3KO* compared with the wild type. The same images used for B and C were analyzed for angle and parallelness (Student's *t* test, $^{**}P < 0.01$). F, Pairwise correlation coefficient was calculated at all possible temporal spacings from time-lapse series of epidermal cells in the elongation zone of the root. Filaments in *xi3KO* had significantly reduced overall actin dynamicity compared with the wild type. Values given are means ± SE ($n \geq 35$ cells from 15 seedlings per genotype; ANOVA, $P < 0.01$).

cells: filament translocation and buckling, and filament turnover by assembly and disassembly events (Staiger et al., 2009; Smertenko et al., 2010; Henty-Ridilla et al., 2013). To dissect the mechanisms through which Arabidopsis myosin XI regulates actin rearrangements, we tracked the dynamic behavior of single actin filaments in time-lapse VAEM series collected from hypocotyl epidermal cells (Staiger et al., 2009).

An in vitro reconstituted system was used to show that skeletal muscle myosin II could induce the disassembly and fragmentation of actin filaments (Murrell and Gardel, 2012; Vogel et al., 2013). We hypothesize that the loss of myosin XI would cause a decrease in actin turnover in Arabidopsis epidermal cells. As shown in Table I, actin filaments in *xi3KO* mutant cells showed a decrease in severing frequency to about one-half of the wild-type level, as well as a 50% increase in maximum filament length and an almost 2-fold increase in maximum filament lifetime. These results demonstrate that actin turnover was reduced in the *xi3KO* mutant, because in Arabidopsis epidermal cells, actin filament disassembly is mainly achieved through severing activity (Staiger et al., 2009; Henty et al., 2011).

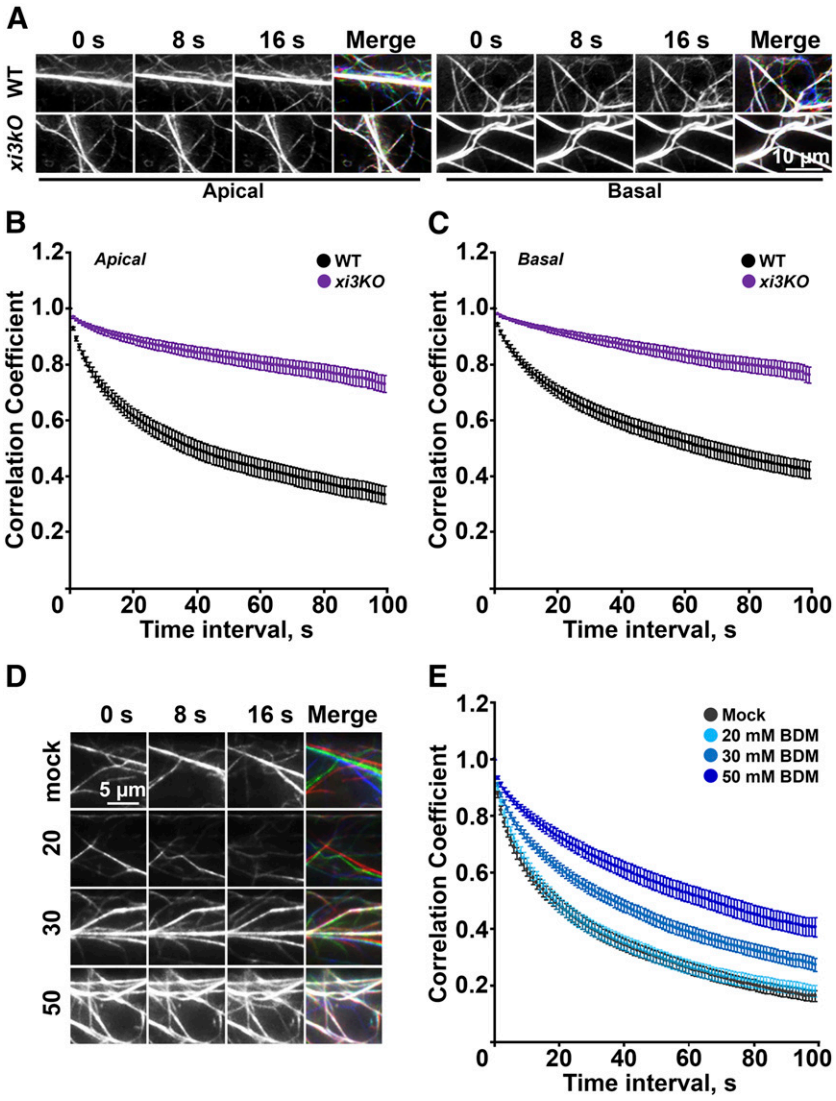

Figure 4. Overall actin dynamicity is reduced in the *xi3KO* mutant and BDM-treated epidermal cells. A, Representative time-lapse VAEM images taken from 5-d-old dark-grown hypocotyls of wild-type (WT) and *xi3KO* Arabidopsis seedlings expressing YFP-fABD2. Images shown were taken from epidermal cells in the apical and basal regions of the hypocotyl and displayed at 8-s intervals. The merged image shows the three time points in separate colors (red, green, and blue). Bar = 10 μm. B and C, Pairwise correlation coefficient was calculated at all possible temporal spacings from time-lapse series collected at the apical (B) and basal (C) regions of the hypocotyl. Filaments in *xi3KO* had reduced overall actin dynamicity compared with the wild type. Values given are means ± SE ($n \geq 40$ cells from 10 seedlings per genotype; ANOVA, $P < 0.01$). D, Representative time-lapse VAEM images taken from 5-d-old dark-grown hypocotyls treated with 0 (mock), 20, 30, or 50 mM BDM for 5 min. Images shown were taken from epidermal cells in the basal region of the hypocotyl and displayed at 8-s intervals. Bar = 5 μm. E, Pairwise correlation coefficient was calculated at all possible temporal spacings from time-lapse series collected at the basal region of the hypocotyl. Epidermal cells showed a dose-dependent reduction in overall actin dynamicity. Values given are means ± SE ($n \geq 40$ cells from 10 seedlings per genotype; ANOVA, $P < 0.01$).

In budding yeast, mutation of myosin V causes an apparent reduction in actin cable extension rates, which results from the loss of filament populations that translocated at rates greater than 2 μm s^{-1} (Yu et al., 2011). Given that myosin XI in Arabidopsis is a close relative of yeast myosin V (Hodge and Cope, 2000), we hypothesize that the average filament elongation rate in *xi3KO* would be reduced due to the loss of fast-growing filaments, assuming that filaments with fast elongation rates are actually translocating rather than assembling from monomers. By tracking the behavior of dynamic filament ends, however, no significant change of average filament elongation rate was detected between *xi3KO* and wild-type control cells (Table I; Fig. 5A). We further categorized the filaments into three populations based on elongation rate, as described in Yu et al. (2011). As shown in Figure 5B, the proportion of filaments with different elongation rates was not altered in *xi3KO* compared with the wild type. Unlike the situation in the budding yeast, the fastest population of growing filament ends (>2 μm s^{-1}) remained the same statistically as the wild-type control. Because the actin cable extension measured in Yu et al. (2011) is a combination of elongation and translocation, these results indicate that we probably measured different aspects of actin dynamics from those in yeast. Our results show that these three class XI Arabidopsis myosins are not involved in the regulation of actin assembly.

We also quantified several other single actin filament dynamic parameters to determine whether myosin XI regulates additional aspects of the dynamic behavior, for example, the availability of filament ends (Table I). The regrowth frequency, annealing frequency, and filament origin were not significantly different in *xi3KO* cells compared with the wild type. Collectively, these results indicate that the three class XI Arabidopsis myosins do not have a major effect on the behavior of dynamic filament ends. However, class XI myosins do contribute to filament disassembly through modulation

Table I. *Comparison of actin dynamics parameters from wild-type and xi3KO epidermal cells*

Measurements taken from epidermal cells in 5-d-old hypocotyls of the *xi3KO* mutant and wild-type plants. Values given are means ± SE, with $n > 50$ filaments from $n > 10$ epidermal cells and at least 10 hypocotyls per line. ND, Not significantly different from the wild-type control value by Student's *t* test ($P > 0.05$). *Significantly different from the wild-type control value by Student's *t* test ($P < 0.05$). **Significantly different from the wild-type control value by Student's *t* test ($P < 0.001$). For filament origin, $n > 300$ filament from $n > 30$ epidermal cells and at least 10 hypocotyls per line. ‡, Not significantly different from the wild-type control value by ANOVA ($P > 0.05$).

Stochastic Dynamics Parameters	Wild Type	*xi3KO*
Apical		
Elongation rate ($\mu m\ s^{-1}$)	1.76 ± 0.04	1.78 ± 0.05ND
Filament breaks (breaks)	3.5 ± 0.1	3.8 ± 0.2ND
Severing frequency (breaks $\mu m^{-1}\ s^{-1}$)	0.016 ± 0.001	0.008 ± 0.001**
Max length (μm)	11.2 ± 0.4	15.0 ± 1.0**
Max lifetime (s)	21.1 ± 0.6	37.9 ± 1.8**
Regrowth of severed ends (%)	5.2 ± 1.7	3.3 ± 1.2ND
Annealing of severed ends (%)	3.8 ± 1.5	1.3 ± 0.7ND
Filament origin (% per cell)		
De novo	28.8 ± 3.5	27.5 ± 8.6‡
Ends	21.4 ± 3.9	20.9 ± 7.7‡
Side	49.2 ± 3.1	51.3 ± 5.4‡
Convolutedness	1.25 ± 0.05	1.11 ± 0.01*
Rate of change of convolutedness (s^{-1})	0.09 ± 0.01	0.04 ± 0.003**
Basal		
Elongation rate ($\mu m\ s^{-1}$)	1.79 ± 0.05	1.86 ± 0.05ND
Filament breaks (breaks)	4.7 ± 0.2	4.5 ± 0.2ND
Severing frequency (breaks $\mu m^{-1}\ s^{-1}$)	0.014 ± 0.001	0.007 ± 0.001**
Max length (μm)	12.6 ± 0.4	17.0 ± 0.7**
Max lifetime (s)	27.6 ± 0.8	44.1 ± 1.9**
Regrowth of severed ends (%)	3.3 ± 1.1	3.2 ± 1.2ND
Annealing of severed ends (%)	2.6 ± 1.1	1.2 ± 0.8ND
Filament origin (% per cell)		
De novo	29.5 ± 2.6	28.4 ± 7.1‡
Ends	21.0 ± 3.0	21.7 ± 6.5‡
Side	48.6 ± 3.4	50.6 ± 4.4‡
Convolutedness	1.27 ± 0.04	1.20 ± 0.04ND
Rate of change of convolutedness (s^{-1})	0.09 ± 0.01	0.03 ± 0.003**

of severing frequency, which was reduced 2-fold in the mutant cells.

Myosin XI Generates Force for Filament and Bundle Buckling and Straightening

Cortical actin filaments undergo continuous shape changes, as well as stochastic dynamic turnover (Staiger et al., 2009; Smertenko et al., 2010). It was shown in a previous study that BDM, a myosin ATPase inhibitor, could reduce actin dynamics by inhibiting filament buckling and straightening events (Staiger et al., 2009). To test whether myosin XI contributes to filament buckling and straightening, we examined the shape of actin filaments in VAEM time-lapse series collected from hypocotyl epidermal cells. Actin filaments in wild-type cells showed continuous buckling and straightening events (Fig. 6A, 24 and 30 s); however, in *xi3KO* mutant cells, the shape of actin filaments remained relatively constant (Fig. 6B). To quantitatively assess the shape of actin filaments, we measured convolutedness and the rate of change of convolutedness. Convolutedness is a dimensionless measure of the ratio of filament length divided by the distance of a straight line connecting the plus and minus ends (Smertenko et al., 2010; Fig. 6A). As shown in Figure 6C, the convolutedness of actin filaments showed a modest reduction (apical) or no difference (basal) in *xi3KO* epidermal cells compared with the wild type. However, the *xi3KO* mutant showed an approximately 2- to 3-fold reduction in the rate of change of convolutedness, indicating the filament buckling and straightening is reduced when three myosin XI isoforms are eliminated. We also examined these parameters for actin filament bundles. Similar to single actin filaments, bundles had a significantly reduced rate of change of convolutedness in the *xi3KO* mutant (Fig. 6, E and F). In sum, these results suggest that three class XI myosins regulate not the overall shape but the shape change of actin filaments and bundles.

DISCUSSION

In this study, we dissected the role of three Arabidopsis class XI myosins in organization and dynamics of cortical actin arrays using high spatiotemporal

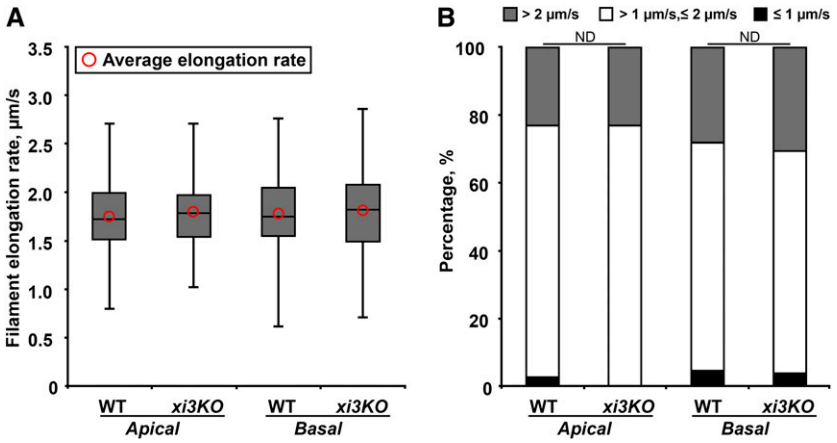

Figure 5. Elongation rate of growing filament ends is not altered in *xi3KO* mutant. A, Box plots show the elongation rate of growing actin filaments in the wild type (WT) and the *xi3KO* mutant. The box spans between the first and the third quartile. The line inside the box shows the median. The bars show the minimum and maximum values. Circles show the average filament elongation rates ($n > 100$ filaments per genotype). B, The elongation rate of growing filaments analyzed in A was binned into three populations: ≤ 1 μm s^{-1}, 1 to 2 μm s^{-1}, and >2 μm s^{-1}. The percentage of each population was calculated. ND indicates not significantly different from wild-type control by χ^2 test ($P > 0.05$). [See online article for color version of this figure.]

resolution imaging of living plant epidermal cells. Arabidopsis myosin XI is important for the expansion of organs and cells at different developmental stages. The *myosin xi-1*, *xi-2*, and *xi-k* triple mutant is a dwarf plant with significantly reduced etiolated hypocotyl length and light-grown root length, as shown previously (Peremyslov et al., 2010). Cell expansion was significantly inhibited in hypocotyls and roots of the *xi3KO* mutant. Moreover, the architecture of cortical actin filament arrays was less dense and more bundled in the *xi3KO* mutant compared with the wild type. These three class XI myosins also contribute to the overall dynamicity of actin in epidermal cells, which is significantly inhibited in the *xi3KO* mutant. This effect on dynamics of actin has two main features: myosin XI promotes the turnover of actin filaments by enhancing severing frequency, and it generates the force for buckling and straightening of single actin filaments and filament bundles. Finally, the three class XI myosins appear not to be involved in regulating the behavior of dynamic filament ends or filament assembly.

The regulation of actin organization by plant myosins has been observed in many studies; however, the results vary in different cell types and based on different methods for inhibiting myosin activity. BDM inhibits the ATPase activity of myosin head domain (Funaki et al., 2004), and its effect on actin filaments in plant cells varies depending on the dose and duration of treatment. Treatment of pollen tubes and root hairs with BDM for 1 h causes a loss of longitudinal orientation of actin bundles in the shank region (Tominaga et al., 2000), whereas short-term treatment (10 min) of growing root hairs with BDM induces the formation of fine actin filament arrays extending into the apical clear zone (Zheng et al., 2009). Due to apparent genetic redundancy within the large gene family, mutants that have multiple *myosin xi* genes knocked out were created to study their function in plant cells (Peremyslov et al., 2008, 2010; Prokhnevsky et al., 2008; Ueda et al., 2010; Ojangu et al., 2012). The Arabidopsis *myosin xi-k, xi-2* double mutant has randomized actin bundle arrays compared with the predominantly longitudinal orientation in wild-type epidermal cells (Ueda et al., 2010). The midvein epidermal cells in triple and quadruple mutants of Arabidopsis *myosin xi* (*xi-1, xi-2, xi-i, xi-k*) lose their longitudinal bundles, and actin filament arrays become more transversely oriented (Peremyslov et al., 2010). Similar to BDM treatment, the actin bundles protrude into the apical clear zone of root hairs in these triple and quadruple mutants (Peremyslov et al., 2010). In tip-growing *P. patens* protonemal cells, actin filament arrays lose their parallel longitudinal orientation and become more randomized when both *Myosin XI* genes are knocked down (Vidali et al., 2010). In this study, we examined the architecture and organization of cortical actin filament arrays in growing and nongrowing epidermal cells from different organs. With quantitative live-cell imaging, we found that the abundance of actin filaments in the cortical array was significantly reduced in the *xi3KO* mutant and that actin filaments were much more bundled compared with the wild type. Moreover, the cortical actin array is more transversely oriented and disorganized in the *xi3KO* mutant compared with the wild type.

In plant cells, actin filament arrays undergo rapid and continuous remodeling (Staiger et al., 2009; Vidali et al., 2009; Smertenko et al., 2010). Recent studies quantified this overall dynamicity of actin arrays to test whether plant myosin XI is involved in the regulation of actin dynamics; however, the results are not consistent between organisms. Knocking down both *Myosin XI* genes in *P. patens* protonemal cells has no effect on the overall actin dynamicity (Vidali et al., 2010), whereas root hairs of the Arabidopsis *myosin xi-k* mutant show a reduction of overall dynamicity of actin filament arrays (Park and Nebenführ, 2013). In this study, we demonstrated that three class XI myosins are important to maintain overall actin dynamicity in diffuse-growing epidermal cells of Arabidopsis. The overall actin dynamicity was significantly inhibited in the *xi3KO* mutant in both growing and nongrowing hypocotyl cells as well as in root elongation zone epidermal cells. In addition, we demonstrated that the myosin ATPase inhibitor BDM inhibits overall actin dynamicity.

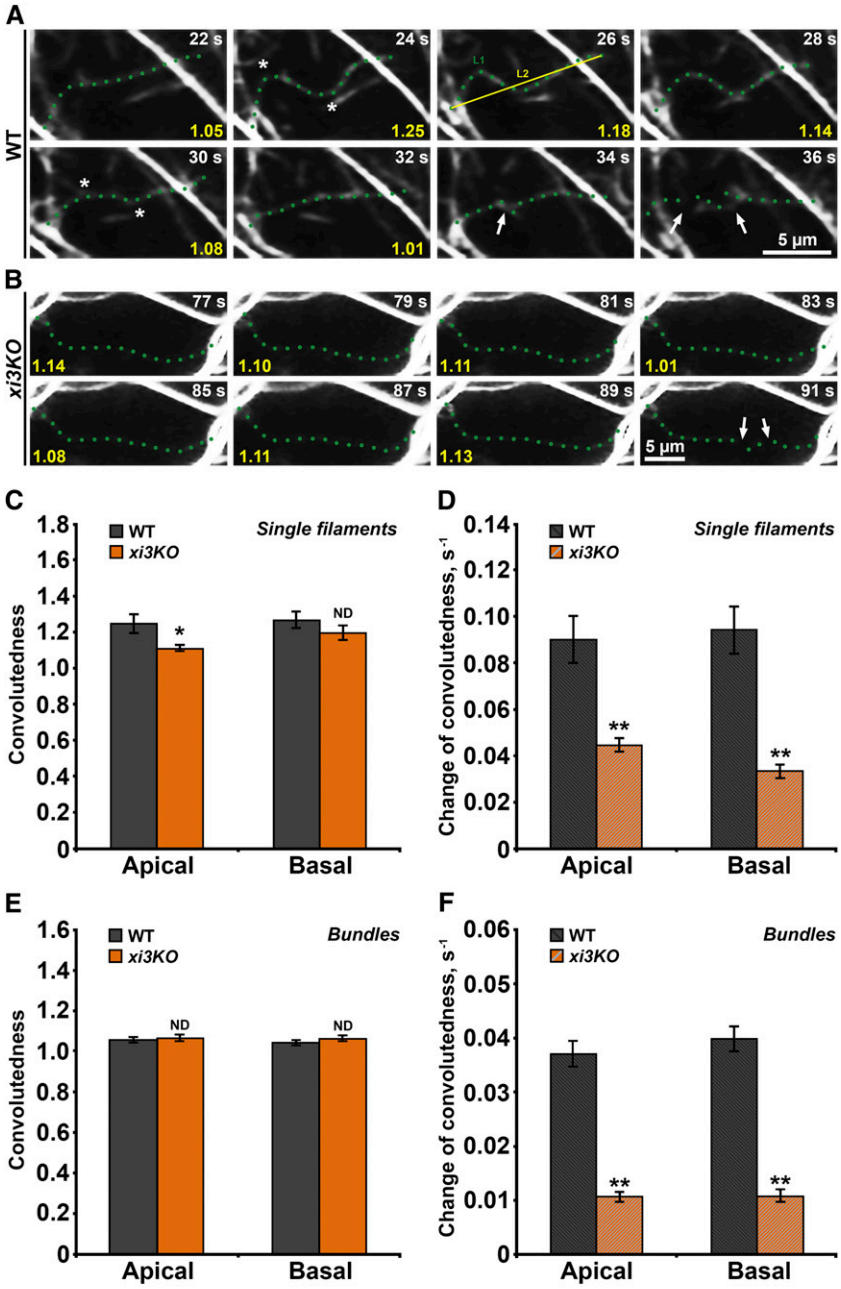

Figure 6. The rate of filament buckling and straightening is reduced in the *xi3KO* mutant. A and B, Time-lapse VAEM series show examples of actin filament buckling and straightening in wild-type (WT) epidermal cells (A) but not in the *xi3KO* mutant cells (B). The filament highlighted in A buckled (asterisks) at two sites at 24 s and straightened (asterisks) at 30 s and then got severed at 34 and 36 s (arrows). However, the filament highlighted in B showed no visible shape change during the entire time series and eventually got severed at 91 s (arrows). Bar = 5 μm. C and D, Quantitative analyses of single actin filament shape change in wild-type and *xi3KO* mutant epidermal cells. C, Convolutedness was measured as the ratio of filament length (L1) divided by the Euclidean distance (L2), as shown in A. Values for the representative filaments are stamped in yellow in A and B. Convolutedness showed a modest reduction at the apical region of the hypocotyl but no significant difference in *xi3KO* compared with the wild type at the base of hypocotyls ($n \geq 50$ filaments from 10 hypocotyls per genotype; Student's *t* test, $*0.01 < P < 0.05$). D, Rate of change of convolutedness of single actin filaments was measured. The rate of change of convolutedness was significantly decreased in cells from both apical and basal regions of hypocotyls in the *xi3KO* mutant compared with the wild type. Values given are means ± SE. The same images used for C were analyzed for D (Student's *t* test, $**P < 0.01$). E and F, Quantitative analyses of actin bundle shape change in wild-type and *xi3KO* mutant epidermal cells. E, Convolutedness of actin filament bundles showed no significant difference in *xi3KO* compared with the wild type at either the apical or basal region of hypocotyls ($n \geq 50$ bundles from 10 hypocotyls per genotype; Student's *t* test, $*0.01 < P < 0.05$). F, The rate of change of convolutedness of actin filament bundles was significantly decreased in cells from both apical and basal regions of hypocotyls in the *xi3KO* mutant compared with the wild type. Values given are means ± SE. The same images used for E were analyzed for F (Student's *t* test, $**P < 0.01$). ND, No significant difference.

The dynamic behavior of actin filament arrays is contributed mainly by two features: filament assembly and disassembly, and filament translocation and buckling (Henty-Ridilla et al., 2013; Li et al., 2014a). These properties of actin filaments can be tracked with high-resolution time-lapse imaging (Staiger et al., 2009). Previous data from diverse classes of myosin demonstrate that motors can regulate the dynamics of actin filaments. In budding yeast, myosin V delivers formin regulators, which locally alter the assembly of actin filaments at the bud neck (Chesarone-Cataldo et al., 2011). Further, yeast myosin V enhances actin cable motility by promoting translocation of bundles (Yu et al., 2011). Conventional myosin II from rabbit skeletal muscle is able to induce the fragmentation of actin filaments, which facilitates the turnover of actin in vitro (Murrell and Gardel, 2012; Vogel et al., 2013). Here, by tracking the dynamic behavior of individual actin filaments in vivo, we quantitatively assessed the effects of loss of myosin XI on parameters of stochastic turnover. We found that three Arabidopsis myosins XI are critical for the turnover of actin. In the *xi3KO* mutant, severing frequency was significantly inhibited compared with the wild type, which led to an increase in maximum filament length and lifetime. In this case, myosin might generate tension on filaments that facilitates the action

of other severing proteins. Alternatively, filament buckling by myosin could directly result in breaks along the length of the polymer. Regardless of mechanism, this is the first genetic evidence that myosin is involved in regulating filament fragmentation and actin turnover in plant cells.

Myosin XI appears not to be involved in regulating filament ends or filament assembly in Arabidopsis epidermal cells. The *myosin xi3KO* mutant did not have altered annealing and regrowth frequencies, which indicates that the number of free filament ends was not changed. Actin filaments originate from different locations (de novo, side, and end), suggesting different mechanisms of nucleation (Staiger et al., 2009). The *xi3KO* mutant did not show any alteration to the proportion of filament origins compared with the wild type. More importantly, in budding yeast, the distribution of distinct populations of actin cables reveals different molecular mechanisms whereby barbed-end elongation is coordinated (Chesarone-Cataldo et al., 2011; Yu et al., 2011). Cable motility rates that are faster than 2 μm s^{-1} are due to filament translocation driven by the type V myosin Myo2p (Yu et al., 2011). Here, we found that there was no significant change in either the average or the distribution of elongation rates in the *xi3KO* mutant. These data indicate that the mechanistically distinct types of elongating barbed ends in plant epidermal cells (Li et al., 2014b) are not regulated by the three class XI myosins and also confirm that the dynamic behavior of filament ends is not regulated by the three class XI myosins.

Filament buckling and straightening is another important feature that contributes to the dynamics of actin filament arrays. A previous study using BDM showed that plant myosin may generate the force for buckling and straightening of actin filaments (Staiger et al., 2009). We hypothesize that myosin XI powers filament buckling by facilitating the sliding of antiparallel filaments past each other, by translocation of filaments along membranes, or both (Szymanski and Cosgrove, 2009; Staiger et al., 2009; Henty-Ridilla et al., 2013; Li et al., 2014a). Here, using a genetic approach, we confirmed that three class XI myosins contribute to the shape change of actin filaments. The rate of change of convolutedness was significantly reduced in epidermal cells of the *xi3KO* mutant. Moreover, although the thick actin bundles are less dynamic than single actin filaments (Staiger et al., 2009), the shape change of actin bundles was also inhibited in the *xi3KO* mutant. Thus, this is the first piece of evidence indicating that three class XI myosins generate force for not only single actin filaments, but also actin bundles in plant epidermal cells. Changes in filament and bundle shape could be powered by antiparallel filament sliding, trafficking of endomembrane compartments along actin filaments, translocation of filaments at the plasma membrane, bulk cytoplasmic streaming, or all of the above.

Plant cell expansion depends on the delivery of membranes and cell wall materials (Smith and Oppenheimer, 2005; Li et al., 2014a). One component of this delivery mechanism is cargo selection. For example, the trafficking of noncellulosic cell wall components is assumed to depend on actin and myosin (Nebenführ et al., 1999). Arabidopsis myosin XI facilitates the motility of secretory vesicles, and a novel cargo adaptor protein was recently identified (Peremyslov et al., 2012, 2013). The other key aspect in myosin-dependent secretion is actin track organization. Proper actin organization is important for the patterning and lifetime of cellulose synthase complex residency at the plasma membrane, which, in turn, impacts crystalline cellulose deposition (Sampathkumar et al., 2013). In this context, anchored myosin motors might generate forces on the actin bundles that support transvacuolar strands and create stable transport pathways to particular locations at the cortex (Szymanski and Cosgrove, 2009). Studying mutants of other conserved actin-binding proteins revealed a correlation between certain actin filament features and cell expansion (Smith and Oppenheimer, 2005; Hussey et al., 2006; Li et al., 2014a). It is hypothesized that longer filament length and increased lifetime enhance axial cell expansion by establishing more efficient tracks for vesicle trafficking (Henty-Ridilla et al., 2013; Li et al., 2014a, 2014b). Our data show that in the *xi3KO* mutant, filament length and lifetime were increased due to the inhibition of severing frequency. However, although filament length and lifetime are increased, cell length and width in the *xi3KO* mutant were reduced. This could suggest that myosin XI is downstream of actin length and lifetime in regulating cell expansion. In other words, track length and lifetime are not relevant when the motors and cargo delivery are inhibited. Moreover, a recent study shows that the velocity of myosin positively correlates with cell size by replacing the ATPase head domain with faster and slower motors (Tominaga et al., 2013). Such mutants provide a unique opportunity to study, in more detail, the relationship between myosin motor activity and actin tracks. For example, it should be possible to test whether the change of myosin velocity would affect turnover of actin filaments or whether a higher velocity of myosin would generate more force for filament buckling and straightening, or both.

MATERIALS AND METHODS

Plant Material and Growth Conditions

The Arabidopsis (*Arabidopsis thaliana*) *xi3KO* mutant and *xi3KO* mutant expressing vYFP-fABD2 were characterized previously (Peremyslov et al., 2010). Seeds were surface sterilized and stratified at 4°C for 3 d on one-half-strength Murashige and Skoog medium. For dark-grown hypocotyls, seedlings were grown on medium supplemented with 1% (w/v) Suc and 1% (w/v) agar. After 4 h of exposure to light, plates were wrapped in three layers of aluminum foil and placed in continuous darkness. For light-grown seedlings, seeds were plated on one-half-strength Murashige and Skoog medium supplemented with 0% (w/v) Suc and 0.6% (w/v) agar (Dyachok et al., 2011; Li et al., 2012). Seedlings were grown vertically under long-day conditions (16 h of light/8 h of dark) at 21°C. To measure the epidermal cell length and width, 5-d-old dark-grown hypocotyls were incubated in 5 μM FM4-64 dye (Invitrogen) for 10 min. Seven-day-old light-grown roots were incubated in 5 μM FM4-64 dye for 5 min. The apical and basal third of hypocotyls and the root

elongation zone were imaged with a 20×/0.25 numerical aperture (NA) objective on a Zeiss Observer Z.1. Wide-field fluorescence micrographs were collected with a charge-coupled device (CCD) camera (QuantEM:512SC; Photometrics). A double-blind experimental design was used for all phenotypic analysis. All image measurements were performed with ImageJ (http://rsb.info.nih.gov/ij/). Data analysis and statistical tests were performed with Microsoft Excel.

VAEM Imaging

VAEM was performed using a total internal reflection fluorescence (TIRF) illuminator on an IX-71 microscope equipped with a 60×/1.45 NA PlanApo TIRF objective (Olympus). YFP-fABD2 was excited with a 488-nm laser line from a solid-state 50-mW laser (Intelligent Imaging Innovations). The emission went through a 525/30-nm filter and was captured with an electron-multiplying CCD camera (ORCA-EM C9100-12; Hamamatsu Photonics). The VAEM platform was operated with Slidebook software (version 5.5.0; Intelligent Imaging Innovations). For the imaging of BDM-treated GFP-fABD2 seedlings, VAEM was performed using a TIRF illuminator on a Zeiss Observer Z.1 equipped with a 100×/1.46 NA PlanApo objective. GFP-fABD2 was excited with a 488-nm laser line from a solid-state 50-mW laser (Intelligent Imaging Innovations). The emission was captured with an electron-multiplying CCD camera (QuantEM:512SC; Photometrics).

Quantitative Analysis of the Architecture of Cortical Actin Arrays

Two parameters, filament abundance (density) and the extent of filament bundling (skewness), were measured as described previously (Higaki et al., 2010; Henty et al., 2011; Li et al., 2012). VAEM snapshots were collected from hypocotyl or root epidermal cells expressing YFP-fABD2 with a fixed laser power, exposure time, and gain setting. Micrographs were cropped and analyzed with ImageJ. At least 150 images of hypocotyl epidermal cells per region, or over 60 images of the root elongation zone from 30 individual seedlings, were collected and analyzed.

Actin Filament Dynamics

VAEM time-lapse series were collected to measure the dynamics of cortical actin arrays in epidermal cells as described previously (Staiger et al., 2009; Henty et al., 2011; Li et al., 2012). Epidermal cells from the apical or basal third of 5-d-old dark-grown hypocotyls or from the root elongation zone of 7-d-old light-grown seedlings were examined. Parameters describing actin turnover and the behavior of filament ends were measured as described (Staiger et al., 2009; Henty et al., 2011; Li et al., 2012). Convolutedness and the rate of change of convolutedness were measured after the actin filament stopped growing. Convolutedness is defined as the ratio of filament length divided by the distance between the plus and minus ends (Smertenko et al., 2010). The rate of change of convolutedness is the average difference in convolutedness between consecutive frames divided by the average time interval between frames. A double-blind experimental design was used to compare the dynamic parameters between genotypes. The time-lapse VAEM images for single filament dynamic measurements were also used for correlation coefficient analyses (Vidali et al., 2010). Images were cropped and analyzed in MATLAB (version 7.14.0, MathWorks) using the method described previously (Vidali et al., 2010).

Supplemental Data

The following materials are available in the online version of this article.

Supplemental Figure S1. Overall actin dynamicity of both single actin filament and actin bundles is reduced in the *xi3KO* mutant.

Supplemental Methods S1. Overall dynamicity analysis for single actin filaments and actin bundles.

ACKNOWLEDGMENTS

We thank Dr. Valerian Dolja (Oregon State University) for kindly providing the *xi3KO* and *xi3KO*;YFP-fABD2 seeds, Benjamin H. Staiger (Purdue University) for customizing the actin architecture and correlation coefficient analysis tools, and Hongbing Luo (Purdue University) for excellent care and maintenance of plant materials. The TIRF microscopy facility was funded in part by the Bindley Bioscience Center, Purdue University.

Received June 2, 2014; accepted September 17, 2014; published September 18, 2014.

LITERATURE CITED

Avisar D, Abu-Abied M, Belausov E, Sadot E, Hawes C, Sparkes IA (2009) A comparative study of the involvement of 17 Arabidopsis myosin family members on the motility of Golgi and other organelles. Plant Physiol **150:** 700–709

Avisar D, Prokhnevsky AI, Makarova KS, Koonin EV, Dolja VV (2008) Myosin XI-K is required for rapid trafficking of Golgi stacks, peroxisomes, and mitochondria in leaf cells of *Nicotiana benthamiana*. Plant Physiol **146:** 1098–1108

Chesarone-Cataldo M, Guérin C, Yu JH, Wedlich-Soldner R, Blanchoin L, Goode BL (2011) The myosin passenger protein Smy1 controls actin cable structure and dynamics by acting as a formin damper. Dev Cell **21:** 217–230

Dyachok J, Zhu L, Liao F, He J, Huq E, Blancaflor EB (2011) SCAR mediates light-induced root elongation in *Arabidopsis* through photoreceptors and proteasomes. Plant Cell **23:** 3610–3626

Funaki K, Nagata A, Akimoto Y, Shimada K, Ito K, Yamamoto K (2004) The motility of *Chara corallina* myosin was inhibited reversibly by 2,3-butanedione monoxime (BDM). Plant Cell Physiol **45:** 1342–1345

Gendreau E, Traas J, Desnos T, Grandjean O, Caboche M, Höfte H (1997) Cellular basis of hypocotyl growth in *Arabidopsis thaliana*. Plant Physiol **114:** 295–305

Henty JL, Bledsoe SW, Khurana P, Meagher RB, Day B, Blanchoin L, Staiger CJ (2011) *Arabidopsis* actin depolymerizing factor4 modulates the stochastic dynamic behavior of actin filaments in the cortical array of epidermal cells. Plant Cell **23:** 3711–3726

Henty-Ridilla JL, Li J, Blanchoin L, Staiger CJ (2013) Actin dynamics in the cortical array of plant cells. Curr Opin Plant Biol **16:** 678–687

Herrmann C, Wray J, Travers F, Barman T (1992) Effect of 2,3-butanedione monoxime on myosin and myofibrillar ATPases. An example of an uncompetitive inhibitor. Biochemistry **31:** 12227–12232

Higaki T, Kutsuna N, Sano T, Kondo N, Hasezawa S (2010) Quantification and cluster analysis of actin cytoskeletal structures in plant cells: role of actin bundling in stomatal movement during diurnal cycles in Arabidopsis guard cells. Plant J **61:** 156–165

Hodge T, Cope MJTV (2000) A myosin family tree. J Cell Sci **113:** 3353–3354

Hussey PJ, Ketelaar T, Deeks MJ (2006) Control of the actin cytoskeleton in plant cell growth. Annu Rev Plant Biol **57:** 109–125

Li J, Arieti R, Staiger CJ (2014a) Actin filament dynamics and their role in plant cell expansion. *In* H Fukuda, ed, Plant Cell Wall Patterning and Cell Shape. John Wiley and Sons, Hoboken, NJ, pp 127–162

Li J, Henty-Ridilla JL, Huang S, Wang X, Blanchoin L, Staiger CJ (2012) Capping protein modulates the dynamic behavior of actin filaments in response to phosphatidic acid in *Arabidopsis*. Plant Cell **24:** 3742–3754

Li J, Staiger BH, Henty-Ridilla JL, Abu-Abied M, Sadot E, Blanchoin L, Staiger CJ (2014b) The availability of filament ends modulates actin stochastic dynamics in live plant cells. Mol Biol Cell **25:** 1263–1275

McCurdy DW (1999) Is 2,3-butanedione monoxime an effective inhibitor of myosin-based activities in plant cells? Protoplasma **209:** 120–125

Murrell MP, Gardel ML (2012) F-actin buckling coordinates contractility and severing in a biomimetic actomyosin cortex. Proc Natl Acad Sci USA **109:** 20820–20825

Nebenführ A, Gallagher LA, Dunahay TG, Frohlick JA, Mazurkiewicz AM, Meehl JB, Staehelin LA (1999) Stop-and-go movements of plant Golgi stacks are mediated by the acto-myosin system. Plant Physiol **121:** 1127–1142

Ojangu EL, Tanner K, Pata P, Järve K, Holweg CL, Truve E, Paves H (2012) Myosins XI-K, XI-1, and XI-2 are required for development of pavement cells, trichomes, and stigmatic papillae in Arabidopsis. BMC Plant Biol **12:** 81

Park E, Nebenführ A (2013) Myosin XIK of *Arabidopsis thaliana* accumulates at the root hair tip and is required for fast root hair growth. PLoS ONE **8:** e76745

Peremyslov VV, Klocko AL, Fowler JE, Dolja VV (2012) Arabidopsis myosin XI-K localizes to the motile endomembrane vesicles associated with F-actin. Front Plant Sci **3:** 184

Peremyslov VV, Morgun EA, Kurth EG, Makarova KS, Koonin EV, Dolja VV (2013) Identification of myosin XI receptors in *Arabidopsis* defines a distinct class of transport vesicles. Plant Cell **25:** 3022–3038

Peremyslov VV, Prokhnevsky AI, Avisar D, Dolja VV (2008) Two class XI myosins function in organelle trafficking and root hair development in Arabidopsis. Plant Physiol **146:** 1109–1116

Peremyslov VV, Prokhnevsky AI, Dolja VV (2010) Class XI myosins are required for development, cell expansion, and F-Actin organization in *Arabidopsis*. Plant Cell **22:** 1883–1897

Prokhnevsky AI, Peremyslov VV, Dolja VV (2008) Overlapping functions of the four class XI myosins in Arabidopsis growth, root hair elongation, and organelle motility. Proc Natl Acad Sci USA **105:** 19744–19749

Šamaj J, Peters M, Volkmann D, Baluška F (2000) Effects of myosin ATPase inhibitor 2,3-butanedione 2-monoxime on distributions of myosins, F-actin, microtubules, and cortical endoplasmic reticulum in maize root apices. Plant Cell Physiol **41:** 571–582

Sampathkumar A, Gutierrez R, McFarlane HE, Bringmann M, Lindeboom J, Emons AM, Samuels L, Ketelaar T, Ehrhardt DW, Persson S (2013) Patterning and lifetime of plasma membrane-localized cellulose synthase is dependent on actin organization in Arabidopsis interphase cells. Plant Physiol **162:** 675–688

Schuh M (2011) An actin-dependent mechanism for long-range vesicle transport. Nat Cell Biol **13:** 1431–1436

Smertenko AP, Deeks MJ, Hussey PJ (2010) Strategies of actin reorganisation in plant cells. J Cell Sci **123:** 3019–3028

Smith LG, Oppenheimer DG (2005) Spatial control of cell expansion by the plant cytoskeleton. Annu Rev Cell Dev Biol **21:** 271–295

Sparkes IA, Teanby NA, Hawes C (2008) Truncated myosin XI tail fusions inhibit peroxisome, Golgi, and mitochondrial movement in tobacco leaf epidermal cells: a genetic tool for the next generation. J Exp Bot **59:** 2499–2512

Staiger CJ, Sheahan MB, Khurana P, Wang X, McCurdy DW, Blanchoin L (2009) Actin filament dynamics are dominated by rapid growth and severing activity in the Arabidopsis cortical array. J Cell Biol **184:** 269–280

Szymanski DB, Cosgrove DJ (2009) Dynamic coordination of cytoskeletal and cell wall systems during plant cell morphogenesis. Curr Biol **19:** R800–R811

Tominaga M, Kimura A, Yokota E, Haraguchi T, Shimmen T, Yamamoto K, Nakano A, Ito K (2013) Cytoplasmic streaming velocity as a plant size determinant. Dev Cell **27:** 345–352

Tominaga M, Yokota E, Sonobe S, Shimmen T (2000) Mechanism of inhibition of cytoplasmic streaming by a myosin inhibitor, 2,3-butanedione monoxime. Protoplasma **213:** 46–54

Ueda H, Yokota E, Kutsuna N, Shimada T, Tamura K, Shimmen T, Hasezawa S, Dolja VV, Hara-Nishimura I (2010) Myosin-dependent endoplasmic reticulum motility and F-actin organization in plant cells. Proc Natl Acad Sci USA **107:** 6894–6899

Vidali L, Burkart GM, Augustine RC, Kerdavid E, Tüzel E, Bezanilla M (2010) Myosin XI is essential for tip growth in *Physcomitrella patens*. Plant Cell **22:** 1868–1882

Vidali L, Rounds CM, Hepler PK, Bezanilla M (2009) Lifeact-mEGFP reveals a dynamic apical F-actin network in tip growing plant cells. PLoS ONE **4:** e5744

Vogel SK, Petrasek Z, Heinemann F, Schwille P (2013) Myosin motors fragment and compact membrane-bound actin filaments. eLife **2:** e00116

Yu JH, Crevenna AH, Bettenbühl M, Freisinger T, Wedlich-Söldner R (2011) Cortical actin dynamics driven by formins and myosin V. J Cell Sci **124:** 1533–1541

Zheng M, Beck M, Müller J, Chen T, Wang X, Wang F, Wang Q, Wang Y, Baluška F, Logan DC, et al (2009) Actin turnover is required for myosin-dependent mitochondrial movements in Arabidopsis root hairs. PLoS ONE **4:** e5961